MARTIN MARIETTA ENERGY SYSTEMS LIBRARIES
3 4456 0361378 4

CRL

4

CENTRAL RESEARCH LIBRARY
DOCUMENT COLLECTION

ORNL-2732
Physics and Mathematics

MEASUREMENT OF ELECTRON FLUX IN IRRADIATED MEDIA BY AC METHODS

R. A. Finston
H. H. Hubbell, Jr.
W. G. Stone
R. D. Birkhoff

CENTRAL RESEARCH LIBRARY
DOCUMENT COLLECTION
LIBRARY LOAN COPY
DO NOT TRANSFER TO ANOTHER PERSON
If you wish someone else to see this document, send in name with document and the library will arrange a loan.

OAK RIDGE NATIONAL LABORATORY
operated by
UNION CARBIDE CORPORATION
for the
U.S. ATOMIC ENERGY COMMISSION

LEGAL NOTICE

This report was prepared as an account of Government sponsored work. Neither the United States, nor the Commission, nor any person acting on behalf of the Commission:

A. Makes any warranty or representation, expressed or implied, with respect to the accuracy, completeness, or usefulness of the information contained in this report, or that the use of any information, apparatus, method, or process disclosed in this report may not infringe privately owned rights; or

B. Assumes any liabilities with respect to the use of, or for damages resulting from the use of any information, apparatus, method, or process disclosed in this report.

As used in the above, "person acting on behalf of the Commission" includes any employee or contractor of the Commission, or employee of such contractor, to the extent that such employee or contractor of the Commission, or employee of such contractor prepares, disseminates, or provides access to, any information pursuant to his employment or contract with the Commission, or his employment with such contractor.

ORNL-2732

Contract No. W-7405-eng-26

HEALTH PHYSICS DIVISION

MEASUREMENT OF ELECTRON FLUX IN IRRADIATED MEDIA BY AC METHODS

R. A. Finston
H. H. Hubbell, Jr.
W. G. Stone
R. D. Birkhoff

Submitted as a thesis to the Faculty of the Graduate School of Vanderbilt University in partial fulfillment of the requirements for the degree of Master of Science in Physics.

DATE ISSUED

Sept. 1959

OAK RIDGE NATIONAL LABORATORY
Oak Ridge, Tennessee
operated by
UNION CARBIDE CORPORATION
for the
U. S. ATOMIC ENERGY COMMISSION

MARTIN MARIETTA ENERGY SYSTEMS LIBRARIES

3 4456 0361378 4

ACKNOWLEDGMENTS

I am indebted to R. D. Birkhoff, H. H. Hubbell, Jr., and R. M. Johnson for their direction and advice on this research. To W. G. Stone go many thanks for the design of the basic circuitry and preliminary investigation of the AC measurement technique. Thanks are also due to J. A. Harter for his help and counsel in electronics problems, and to E. Fairstein for assistance in circuit analysis.

I wish to express my grateful appreciation to E. E. Anderson for the active interest she has taken in my graduate studies and to W. W. Gregorieff and the Oak Ridge Institute of Nuclear Studies for providing an A.E.C. Radiological Physics Fellowship.

TABLE OF CONTENTS

	Page
Acknowledgments	ii
List of Tables	v
List of Figures	vi
I. Introduction	1
II. Theory	4
A. Generation of Secondary Electrons in Media	4
B. Parallel-Plate Spectrometer	5
C. AC Measurement of the Derivatives of the Current-Voltage Curve	11
1. The problem and earlier solutions	11
2. Inter-modulation technique for determination of d^2I/dV^2	14
3. Energy resolution of AC measurements	19
III. Apparatus	29
A. X-Ray Machine	29
B. Parallel-Plate Spectrometer	31
C. Low-Noise Pre-amplifier	34
1. General description of the circuit	34
a. Sources of noise	34
b. Parameters and techniques for reduction of noise due to external sources	35
c. Parameters and techniques for reduction of inherent noise	38
d. Selection of circuit	43
e. Selection of tubes and practical operating parameters	49

TABLE OF CONTENTS CON'T

	Page
2. Construction	51
a. Electrical	51
b. Mechanical	53
D. Electrical Circuit	56
1. Input	56
a. Signal generators	56
b. Mixing network and balancing circuit	56
c. Pre-amplifier input network	59
2. Output	59
a. DC current electrometer	59
b. AC voltage wave analyzer	60
E. Vacuum System	60
IV. Experimental Procedure and Data Analysis	63
A. Experimental Procedure	63
B. Data Analysis	65
V. Experimental Results	69
A. Energy Spectra	69
B. Saturation Current Density	80
VI. Conclusions	91
Appendix	
I. Error Analysis	92
II. Table VII. Fermi Energy, E_F and Photoelectric Work Function ϕ for Cu, Al, Graphite, and Tissue Equivalent Conducting Plastic	94
Bibliography	95

LIST OF TABLES

		Page
I.	Calculations of Spectrometer Plate Thickness	33
II.	Energy Distribution of Flux in Annealed Copper	81
III.	Energy Distribution of Flux in Aluminum	82
IV.	Energy Distribution of Flux in Graphite	83
V.	Energy Distribution of Flux in Conducting Tissue Equivalent Plastic	84
VI.	Current Densities at Saturation	85
VII.	Fermi Energy and Photoelectric Work Function Φ for Copper, Aluminum, Graphite, and Tissue Equivalent Conducting Plastic	94

LIST OF FIGURES

No.		Page
1.	Schematic Diagram of Apparatus for Determining the Flux of Electrons in Irradiated Matter	6
2.	Current-Voltage Curve and Derivatives for Monoenergetic Electrons	21
3.	Phase Angle Analysis and Monoenergetic Electron Line Profile	23
4.	Line Profile of Parallel-Plate Spectrometer for Monoenergetic Electrons	28
5.	X-Ray Head and Vacuum System Enclosure	30
6.	Parallel-Plate Spectrometer Cross Section	32
7.	Low-Noise Pre-amplifier Circuit	48
8.	Plate Current of Output Stage vs. Grid Voltage of Pre-amplifier Input Stage	52
9.	Low-Noise Pre-amplifier Assembly	54
10.	Parallel-Plate Spectrometer and Pre-amplifier	55
11.	Circuit Schematic Diagram	58
12.	High Vacuum as a Function of Forepump "Off" Time	62
13.	Current-Voltage Curve for Annealed Copper, (250 KVCP X-Rays)	70
14.	First Derivative of Current-Voltage Curve for Annealed Copper, (250 KVCP X-Rays)	71
15.	Second Derivative of Current-Voltage Curve for Annealed Copper, (250 KVCP X-Rays)	72
16.	Energy Distribution of Flux in Annealed Copper	73
17.	Energy Distribution of Flux in Aluminum	74
18.	Energy Distribution of Flux in Graphite	75
19.	Energy Distribution of Flux in Tissue Equivalent Conducting Plastic	76
20.	Comparison of Energy Distribution for Annealed Copper (250 KVCP X-Rays) with Nelson's Data	77

LIST OF FIGURES (Cont.)

No.		Page
21.	Comparison of Energy Distribution for Aluminum (250 KVCP X-Rays) with Nelson's Data	78
22.	Comparison of Energy Distribution for Graphite (250 KVCP X-Rays) with Nelson's Data	79
23.	Saturation Current Density per Roentgen for Heavily Filtered X-Rays	88
24.	Saturation Current Density per Absorbed Rad for Heavily Filtered X-Rays	89

ABSTRACT

The low energy secondary electron flux generated within a medium under X-irradiation was determined by measuring the derivatives of the current voltage curve of two closely spaced parallel plates irradiated in vacuum. Previously the derivatives had been evaluated directly from the current-voltage curve in work reported by Nelson, Birkhoff, Ritchie and Hubbell. Now considerably increased accuracy, sensitivity, and electron energy range are obtained by an AC method. Two signals of equal amplitude and frequencies 300 and 324 c.p.s. modulate the parallel plate DC bias. The beat frequency amplitude appearing in the secondary electron current is directly proportional to the second derivative of the current-voltage curve. First derivatives were obtained by integrating the second derivatives. The energy spectrum of the electron flux can be immediately calculated from the first and second derivatives.

The electron flux spectrum has been measured out to 50 electron-volts in copper and aluminum, and 18 electron-volts in graphite and tissue equivalent conducting plastic. The spectra follow the inverse square dependence with energy for the energy range investigated previously by Nelson, et. al. Beyond these energies, the spectra fall off more rapidly than the inverse square of the energy. The total saturation current yield of secondary electrons was measured for heavily filtered X-rays with effective energies ranging from 35 KeV to 200 KeV. The yields were highly energy dependent when measured in terms of esu $cm^{-2}rad^{-1}$ absorbed in air. However, the yields were relatively energy independent from 45 KeV when expressed in terms of esu $cm^{-2}rad^{-1}$

absorbed in the plate media. The yields were 3.1×10^{-4}, 4.9×10^{-4}, 3.9×10^{-4}, 4.2×10^{-4} esu $cm^{-2} rad^{-1}$ absorbed in copper, aluminum, graphite, and tissue equivalent conducting plastic, respectively.

I. INTRODUCTION

The interaction of ionizing radiation with matter is of fundamental importance in the study of radiation damage. Incident X-rays produce high energy Compton electrons and photoelectrons in a material. These primaries are degraded in energy by production of secondary electrons with the result that a relatively large number of low energy secondary and tertiary electrons are formed in the medium. Platzman[1] has emphasized the important role which these low energy electrons may play in radiation physics and radiobiology.

The energy distribution of the secondary electron flux generated by X-irradiation of copper, aluminum, and graphite was determined by Nelson, Birkhoff, Ritchie, and Hubbell[2]. The spectra were obtained by measuring the current produced in a parallel-plate spectrometer under X-ray bombardment in a vacuum. The first and second derivatives of the current versus spectrometer voltage curves were obtained by point-to-point analysis. The electron spectrum within the plate material could be calculated from these derivatives. This method, however, was limited in sensitivity and accuracy. The maximum secondary electron currents under consideration were of the order of 10^{-10} amperes. Determination of increments of current as small as 10^{-14} amperes was not possible with precision. Also, slight fluctuations in the X-ray beam intensity introduced considerable error in the measurements of the derivatives of the current-voltage curve.

---

[1] Platzman, R. L., Rad. Res., 2, 1 (1955).

[2] Nelson, D. R., Birkhoff, R. D., Ritchie, R. H., Hubbell, H. H., Jr., "Measurement of Electron Flux in Media Bombarded by X-rays," ORNL-2521, Oak Ridge National Laboratory, Oak Ridge, Tennessee (1958). Unpublished.

In the present work, a DC bias with small AC components superimposed was applied to the spectrometer. The AC components of the secondary electron current were shown to be directly proportional to the derivatives of the DC current-voltage curve characteristic of the plate material. The accuracy and reproducibility of the energy spectra determinations were greatly improved. In addition, the sensitivity was increased so that current increments two orders of magnitude smaller than those detected previously could be observed. Thus, the electron energy spectra were measured out as far as 50 volts in some cases, whereas the previous measurements were reliable to only about 20 volts.

The energy dependence of the secondary electron yield, given preliminary consideration by Nelson, was further examined. The total yield of secondary electrons using heavily filtered, approximately monochromatic X-rays was of fundamental interest. Taylor[3] had studied this characteristic previously to determine whether the formation of secondary electrons might be used to measure high intensity radiation. The yields as a function of incident air dose are highly dependent on X-ray energy for high Z materials but are energy independent for tissue equivalent materials. It was determined in the present work that the yields as a function of the <u>dose absorbed in the media</u> were relatively energy independent and of the same magnitude for <u>all</u> materials.

---

[3] Taylor, L. S., Brit. J. of Rad., <u>24</u>, No. 278, 67 (1951).

There has been much theoretical interest in the calculation of slowing down spectra[4,5]. It is hoped that a theoretical analysis of the low energy region will be forthcoming; however, none exists at the present.

---

[4] Spencer, L. V., and Fano, U., Phys. Rev., 93, 1172 (1954).

[5] McGinnies, R. T., NBS 597 (1959).

II. THEORY

A. Generation of Secondary Electrons in Media

Incident X-ray photons produce Compton and photoelectrons within a bombarded medium. The generation and flux of low energy electrons produced by Compton and photoelectrons has been studied theoretically by Spencer and Fano[6]. Because of the lack of suitable electron-electron cross sections below 30 KeV there is as yet no theory for the flux spectrum. Goldberger[7] has calculated the cross section for isotropic center of mass scattering on a degenerate Fermi gas. He found that the cross section is reduced by a multiplicative factor, $\left[1 - \frac{7}{5}\frac{E_F}{E}\right]$, due to the exclusion principle, where E is the energy of the incident particle and E_F is the Fermi energy. This result is valid for $E \geq 2E_F$. For $E_F \leq E \leq 2E_F$, Clemtentell and Villi[8] have found that the correction factor is:

$$\left[1 - \frac{7}{5}\frac{E_F}{E} + \frac{2}{5}\frac{E_F}{E}\left(2 - \frac{E}{E_F}\right)^{5/2}\right]$$

This was corroborated by Ritchie, Nelson, and Birkhoff[9]. The former correction was used by Wolff[10] in a study of the electron slowing down spectrum. It is hoped that these correction factors along with further theoretical efforts will result in a theory of electron-electron slowing down at low energies.

---

6 Spencer, L. V., and Fano, U., op. cit.

7 Goldberger, M. L., Phys. Rev., 74, No. 10, 1269 (1948).

8 Clemtentell, E., and Villi, C., Nuovo Cimento, 2, 1, 176 (1955).

9 Ritchie, R. H., Nelson, D. R., and Birkhoff, R. D., "Low Energy Collision with a Fermi-Dirac Gas," ORNL-2590, p. 110. Oak Ridge National Laboratory, Oak Ridge, Tennessee (1958). Unpublished.

10 Wolff, P. A., Phys. Rev., 95, No. 1, 56 (1954).

B. Parallel-Plate Spectrometer

The parallel-plate spectrometer described by Nelson[11] was used in this research for the measurement of secondary electron spectra. The parallel-plate geometry is ideal for such a measurement; that is, the spectrometer constitutes an effectively infinite medium, and is bombarded isotropically. The energy distribution can be obtained simply from the first and second derivatives of the current-voltage curve characteristic of the spectrometer plate medium under irradiation. The assumptions made are, first, that edge effects are negligible because the gap between the collecting plates is small when compared to the plate diameter; and second, that equal numbers of secondary electrons having identical energy and angular distributions are emitted from both upper and lower plates of the spectrometer.

Consider first the parallel plate collecting electrodes when the lower electrode is positive with respect to the upper electrode, as shown in Figure (1). All electrons emitted from the upper negative plate will reach the positive plate. However, a fraction, f, of those emitted from the lower plate which have an energy (V') exceeding the bias potential V will fail to traverse the cavity. This fraction of emitted electrons possessing energy $V' > V$ are those which have $V' \cos^2 \theta < V$. Of course, all electrons with $V' < V$ will fail to traverse the gap from the positive to the negative electrode. Those electrons from the lower plate which fail to reach the upper plate will return to the lower plate and thus constitute no current in

[11] Nelson, D. R., et. al., op. cit.

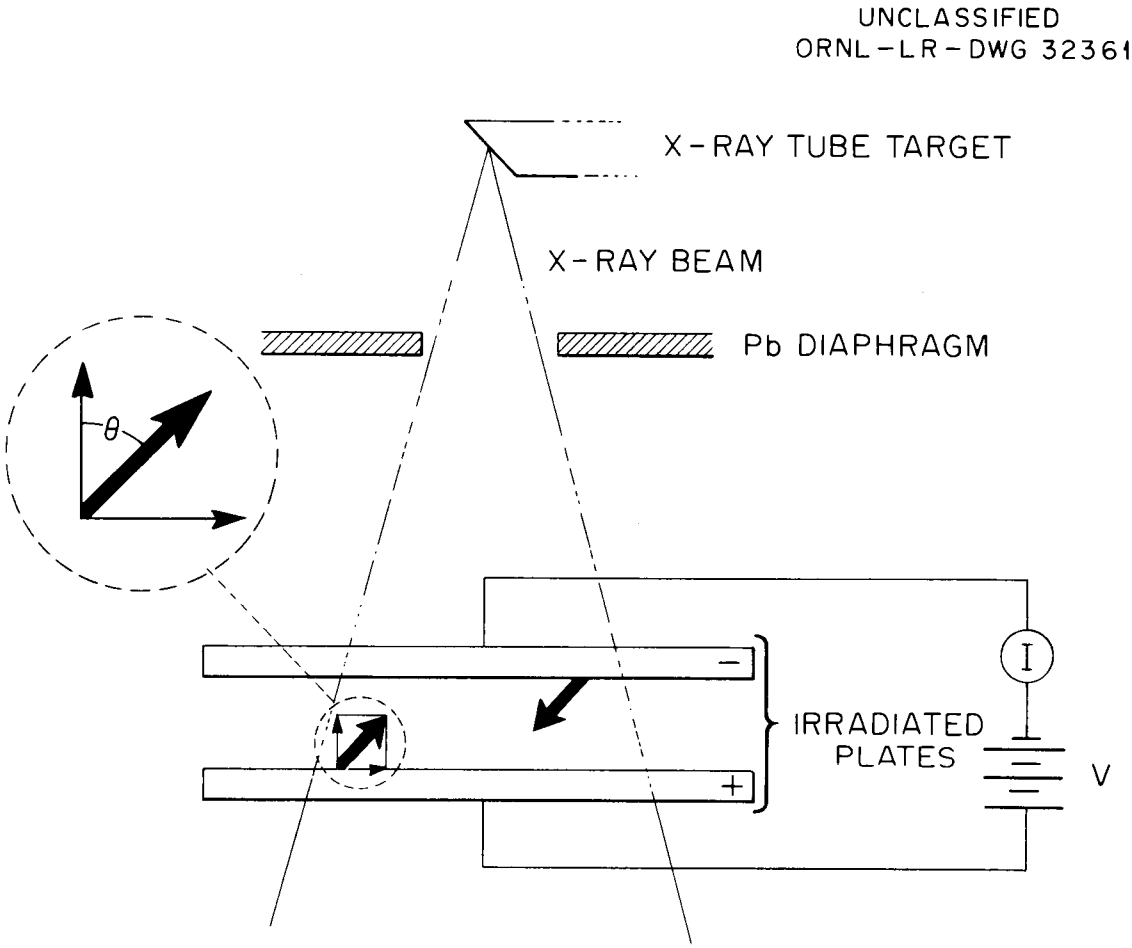

Fig. 1. Schematic Diagram of Apparatus for Determining the Flux of Electrons in Irradiated Matter.

the external circuit. However, their counterparts from the upper plate will cross the gap, and being uncompensated by electrons crossing from the lower plate will produce an external current, I. I can be expressed as:

$$I = eAR \left[\int_0^V N(V')\, dV' + \int_V^\infty f(V,V')\, N(V')\, dV' \right] \qquad (1)$$

where $e = 4.80 \times 10^{-10}$ esu (electronic charge)

A = plate area irradiated (cm^2)

R = dose rate (roentgens/sec.)

$N(V')$ = electron flux from either plate with an energy between V' and $V' + dV'$, in ($cm^{-2}\ r^{-1}\ V^{-1}$)

The first integral represents electrons of energy $V' < V$ which are unable to cross the potential gap from the positive to the negative plate. The second integral represents the fraction, $f(V,V')$, of the electrons with $V' > V$, whose energy associated with the perpendicular component of velocity is less than the energy required to cross the gap.

To determine the energy spectrum of the flux, three possible angular emission distributions of electrons escaping from the plates might be considered: isotropic, cosine and normal. For isotropic emission:

$$f = \alpha \int_{\cos^{-1}\sqrt{V/V'}}^{\pi/2} 2\pi \sin\theta d\theta = 2\pi\, \alpha \sqrt{V/V'} = \sqrt{V/V'} \qquad (2)$$

where $\alpha = 1/2\pi$, the normalization constant for an angular distribution normalized to unity in the 2π solid angle outside the plate.

If the angular emission distribution were cosine:

$$f = \alpha \int_{\cos^{-1}\sqrt{V/V'}}^{\pi/2} 2\pi \cos\theta \sin\theta d\theta = \pi\,\alpha(V/V') = \frac{V}{V'} \qquad (3)$$

where $\alpha = 1/\pi$, the normalization constant to normalize the distribution to unity.

Finally, for emission normal to the surface, $f(V,V') = 0$. That is, all electrons with $V > V'$ would cross the gap, and hence exactly balance their counterparts from the upper electrode and no net current will result from this portion of the energy spectrum.

This information can be generalized by expressing $f(V,V')$ as:

$$f(V,V') = (V/V')^n , \quad V' > V \qquad (4)$$

with $n = 1/2, 1, \infty$ for isotropic, cosine, and normal angular distributions respectively.

The equation for I, the net current becomes:

$$I = eAR \left[\int_0^V N(V')\, dV' + \int_V^\infty (V/V')^n N(V')\, dV' \right] \qquad (5)$$

Differentiating with respect to V gives:

$$\frac{dI}{dV} = eAR \left[N(V) + nV^{n-1} \int_V^\infty (V')^{-n} N(V')dV' - \frac{V^n N(V)}{V^n} \right] \qquad (6)$$

and,

$$\frac{d^2I}{dV^2} = eAR \left[n(n-1)\, V^{n-2} \int_V^\infty (V')^{-n} N(V')\, dV' - nV^{n-1} \frac{N(V)}{V^n} \right] \qquad (7)$$

The solution for N(V) is then

$$N(V) = \frac{1}{eAR} \left[\left(\frac{n-1}{n}\right) \frac{dI}{dV} - \frac{V}{n} \frac{d^2I}{dV^2} \right] \tag{8}$$

For normal emission, $n = \infty$, and

$$N(V) = \frac{1}{eAR} \left(\frac{dI}{dV}\right) . \tag{9}$$

For isotropic emission, $n = 1/2$, and

$$N(V) = \frac{1}{eAR} \left[- \frac{dI}{dV} - 2V \frac{d^2I}{dV^2} \right] . \tag{10}$$

For cosine angular emission, $n = 1$, and

$$N(V) = \frac{1}{eAR} \left[- V \frac{d^2I}{dV^2} \right] . \tag{11}$$

However, the difficulty in determining the angular emission distribution from the plate surface was recognized. Since the primary intent of the experiment was to determine the electron energy spectrum within the medium, a slight alteration of the theoretical problem was undertaken. If it is assumed that the secondary electron flux is isotropic inside the individual plates of the spectrometer, a classical potential-barrier analysis may be undertaken. For a conducting medium the kinetic energy for electrons lying at the bottom of the conduction band is zero. The energy diagram of the parallel-plate geometry would appear as:

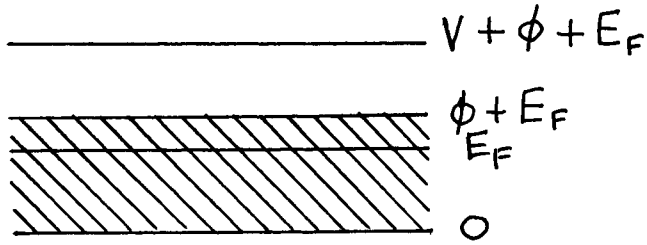

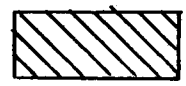
= inside the plate medium

where E_F = Fermi Energy

ϕ = Photoelectric work function

V = Spectrometer bias.

Thus if the Fermi energy and work function are considered as adding to the voltage, V, across which the electron must traverse, then the result obtained by Nelson[12] may be obtained by inspection from equation (10). Hence, for a conducting medium:

$$N(E_F+\phi+V) = \frac{1}{eAR}\left[- \frac{dI}{dV} - 2(E_F + \phi + V)\frac{d^2I}{dV^2}\right] = N(E_w + V), \quad (12)$$

where $E_w = E_F + \phi$.

For a non-conducting medium, $E_F = 0$ and the flux may be represented as:

$$N(\phi + V) = \frac{1}{eAR}\left[- \frac{dI}{dV} - 2(\phi + V)\frac{d^2I}{dV^2}\right] = N(E_w + V). \quad (13)$$

An objection to this interpretation of the current voltage curve, as giving the energy spectrum of secondary electrons, may be raised. It may be argued that the application of the DC bias voltage to the cavity may distort the flux within the cavity. That is, if electrons which would normally produce additional secondaries upon striking a chamber plate were prevented from striking a plate, then the secondaries

[12] Nelson, D. R., et. al., op. cit.

which would normally be born do not occur. However, it has been shown recently[13] that the probability of secondary emission in this energy region is small.

C. AC Measurement of the Derivatives of the Current-Voltage Curve

1. The Problem and Earlier Solutions

In the previous section an expression for the energy spectrum of secondary electrons within the X-ray bombarded medium was discussed. The spectrum can be determined from the first and second derivatives of the current versus voltage curve of the vacuum spectrometer. In the measurements made by Nelson[14], the I versus V curve was measured to a high order of accuracy and the derivatives were then calculated from the data. However, fluctuation in the X-ray beam output, as well as the difficulties inherent in measuring DC current increments as low as 10^{-14} amperes limted the accuracy and sensitivity of the measurements. The X-ray fluctuation might be overcome by use of a gamma source, but a radioisotope source which would deliver a beam 7 cm in diameter and give uniform flux of 4 r/sec could not be easily achieved without a considerable investment in material and shielding.

It was recognized that a direct measurement of the parameters d^2I/dV^2 and dI/dV would improve the accuracy of the experiment. The current voltage curve exhibits non-linearity and the similarity of this non-linear phenomena and that of non-linearity in vacuum tube circuits was apparent. In the latter case, non-linearity of the plate current-grid voltage curves in triodes and pentodes causes distortion of sinusoidal signals applied at the grid.

[13] Fowler, H. A., Farnsworth, H. E., Phys. Rev. 111, No. 1, 103 (1958).
[14] Nelson, D. R., et. al., op. cit.

A paper by Van Der Pol and Weijers[15] describes a method of measuring the successive derivatives of the current-voltage curves in triode operated vacuum tubes. In their work, a pure sinusoidal voltage was impressed on the grid of a triode. If the current-voltage curve was linear, the potential developed across the plate-load resistor would also be pure sine wave. Due to the actual non-linearity of the current-voltage curve, the authors observed several harmonics (up to the tenth) in the potential developed across the plate-load resistor.

A theoretical analysis showed that the amplitudes of the various measured harmonics could be related to the successive derivatives of the current-voltage curve. Assuming that the plate current was an analytic function [$I = f(V)$], of the grid voltage, a Taylor series expansion of the function could be made around the point V_o. Hence, if $V = V_o + a \sin \omega t$, or $(V - V_o) = a \sin \omega t$, were substituted in the expansion, the following expressions for the amplitudes of the plate current were obtained:

Direct Current:

$$I_{DC} = I_o + \frac{a^2}{4}\left(\frac{d^2I}{dV^2}\right)_{V_o} + \frac{a^4}{64}\left(\frac{d^4I}{dV^4}\right)_{V_o} + \frac{a^6}{2304}\left(\frac{d^6I}{dV^6}\right)_{V_o} + \ldots \qquad (14)$$

First Harmonic: ($\sim \sin \omega t$)

$$I_\omega = a\left(\frac{dI}{dV}\right)_{V_o} + \frac{a^3}{8}\left(\frac{d^3I}{dV^3}\right)_{V_o} + \frac{a^5}{192}\left(\frac{d^5I}{dV^5}\right)_{V_o} + \ldots \qquad (15)$$

---

[15] Van Der Pol, Balth, Weijers, Th. J., Physica 1, 481, (1934).

Second Harmonic: ($\sim \cos 2\omega t$)

$$I_{2\omega} = \frac{a^2}{4}\left(\frac{d^2I}{dV^2}\right)_{V_o} + \frac{a^4}{48}\left(\frac{d^4I}{dV^4}\right)_{V_o} + \frac{a^6}{1536}\left(\frac{d^6I}{dV^6}\right)_{V_o} + \ldots \tag{16}$$

Third Harmonic: ($\sim \sin \omega t$)

$$I_{3\omega} = \frac{a^3}{24}\left(\frac{d^3I}{dV^3}\right)_{V_o} + \frac{a^5}{384}\left(\frac{d^5I}{dV^5}\right)_{V_o} + \ldots \tag{17}$$

Fourth Harmonic: ($\sim \cos 4\omega t$)

$$I_{4\omega} = \frac{a^4}{192}\left(\frac{d^4I}{dV^4}\right)_{V_o} + \frac{a^6}{3840}\left(\frac{d^6I}{dV^6}\right)_{V_o} + \ldots \tag{18}$$

When the sinusoidal grid swing (a) is sufficiently small, the amplitudes of the different harmonics of the output current, $I_{n\omega}$, divided by the corresponding power of the amplitude, a^m, converge toward the differentials of the current-voltage curve as:

$$\left(\frac{d^nI}{dV^n}\right)_{V_o} = \lim_{a \to o} 2^{n-1}\, n! \left(\frac{I_n}{a^n}\right) \tag{19}$$

In this method, it is necessary to investigate experimentally whether convergence to a limit does occur for successive reductions of the grid swing (a). A practical test would be to reduce the grid swing 1/3 or 1/10 and observe whether corresponding reductions in plate current occur for the harmonic under consideration. Van der Pol and Weijers found that a convergence was exhibited in the majority of the cases which they considered. Although deviations occurred, such as at points of discontinuity in the function $I = f(V)$, it was felt that

a good approximation for practical work could be obtained, nevertheless, by assuming the function to be analytic. Representation of the characteristic current-voltage function in a series of Tchebycheff polynomials obviated the difficulty of the Taylor series near points of discontinuity. However, measurements would be more complicated for this latter type of representation here and impractical for the determination of the secondary electron spectra. Furthermore, discontinuity in the derivatives of the current-voltage curve of the parallel-plate spectrometer occurred only at zero bias voltage.

2. Intermodulation technique for determination of $\frac{d^2I}{dV^2}$.

It was shown by Nelson[16] that the energy spectrum was predominantly a function of the second derivative of the current-voltage curve for the present case of parallel plate geometry. The first derivative factor was found to contribute 10%, at most, to the spectra calculations. For this reason, a method which would most accurately measure the second derivative was sought.

Two difficulties were evident in the single frequency-harmonic measurement technique. First, the elimination of the AC capacitative current passed to the detector by the capacitance of the parallel-plate spectrometer would require the use of a nulling voltage in the circuit. In this manner only AC currents due to the secondary electron flux would be detected. However, it was found in practice that the null condition could not be maintained for the duration of a spectra measurement. Second, it was found that the magnitude of the impedance

[16] Nelson, D. R., et. al., op. cit.

of the detector grid circuit was limited by the relatively small capacitative reactance to ground. Therefore, to attain the highest possible voltage gain, it was desirable to work at low AC frequencies. Since the oscillators were limited to a minimum of 20 c.p.s. input frequency, the lowest possible second harmonic output frequency which could be used was 40 c.p.s. However, in practice, it was found that a very low noise level existed in the output frequency region of about 20 c.p.s. At this lower frequency the shunting effect of the input grid capacitance would also be less severe.

These considerations led to an investigation of the possibility of an inter-modulation measurement of the second derivatives. In intermodulation distortion measurements of electronic amplifiers, two AC signals are applied to the grid. Non-linearity in the current-voltage curve produces components of plate current with frequency equal to the sum, the difference, the harmonics, etc., of the two applied frequencies. Similarly, if two AC signals were applied to the bias of the parallel-plate spectrometer, non-linearity in the current-voltage curve would give rise to a net current with frequencies representing the sum, difference, harmonics, etc., of the secondary electron current-voltage curve.

Let us consider the function:

$$I = f(V) \tag{20}$$

where I is the current flowing in the spectrometer, and V is the spectrometer bias.

Suppose that

$$V = V_o + A \sin \omega t + B \sin \alpha t \tag{21}$$

where V_o is the DC spectrometer bias and A,B are the amplitudes of the AC modulation at frequencies $\omega/2\pi$, $\alpha/2\pi$ respectively. Then

$$I = f(V_o + A \sin \omega t + B \sin \alpha t) \tag{22}$$

Assuming I is analytic function in the domain considered, then around the point V_o it can be represented as a Taylor series:

$$I = I_o + (A \sin \omega t + B \sin \alpha t) \left(\frac{dI}{dV} \right)_{V_o} + \frac{(A \sin \omega t + B \sin \alpha t)^2}{2!} \left(\frac{d^2 I}{dV^2} \right)_{V_o}$$

$$+ \frac{(A \sin \omega t + B \sin \alpha t)^3}{3!} \left(\frac{d^3 I}{dV^3} \right)_{V_o} + \frac{(A \sin \omega t + B \sin \alpha t)^4}{4!} \left(\frac{d^4 I}{dV^4} \right)_{V_o} \tag{23}$$

$$+ \ldots$$

Expanding this series and collecting like terms in (ω) and (α) gives:

<u>(~ DC)</u>

$$I_{DC} = I_o + \left(\frac{A^2}{4} + \frac{B^2}{4} \right) \left(\frac{d^2 I}{dV^2} \right)_{V_o} + \left(\frac{A^4}{64} + \frac{A^2 B^2}{16} + \frac{B^4}{64} \right) \left(\frac{d^4 I}{dV^4} \right)_{V_o} + \ldots \tag{24}$$

(~ sin ωt)

$$I_\omega = A\left(\frac{dI}{dV}\right)_{V_o} + \left(\frac{A^3}{8} + \frac{AB^2}{4}\right)\left(\frac{d^3I}{dV^3}\right)_{V_o} + \left(\frac{A^5}{192} + \frac{A^3B^2}{32} + \frac{AB^4}{64}\right)\left(\frac{d^5I}{dV^5}\right)_{V_o} + \ldots \tag{25}$$

(~ sin αt)

$$I_\alpha = B\left(\frac{dI}{dV}\right)_{V_o} + \left(\frac{B^3}{8} + \frac{A^2B}{4}\right)\left(\frac{d^3I}{dV^3}\right)_{V_o} + \left(\frac{B^5}{192} + \frac{A^2B^3}{32} + \frac{A^4B}{64}\right)\left(\frac{d^5I}{dV^5}\right)_{V_o} + \ldots \tag{26}$$

(~ cos $(\omega-\alpha)t$)

$$+I_{(\omega-\alpha)} = \frac{AB}{2}\left(\frac{d^2I}{dV^2}\right)_{V_o} + \left(\frac{A^3B}{16} + \frac{AB^3}{16}\right)\left(\frac{d^4I}{dV^4}\right)_{V_o} + \ldots \tag{27}$$

(~ cos $(\omega+\alpha)t$)

$$I_{(\omega+\alpha)} = \frac{AB}{2}\left(\frac{d^2I}{dV^2}\right)_{V_o} + \left(\frac{A^3B}{16} + \frac{AB^3}{16}\right)\left(\frac{d^4I}{dV^4}\right)_{V_o} + \ldots \tag{28}$$

(~ cos $2\omega t$)

$$I_{2\omega} = \frac{A^2}{4}\left(\frac{d^2I}{dV^2}\right)_{V_o} + \left(\frac{A^4}{48} + \frac{A^2B^2}{16}\right)\left(\frac{d^4I}{dV^4}\right)_{V_o} + \ldots \tag{29}$$

(~ cos $2\alpha t$)

$$I_{2\alpha} = \frac{B^2}{4}\left(\frac{d^2I}{dV^2}\right)_{V_o} + \left(\frac{B^4}{48} + \frac{A^2B^2}{16}\right)\left(\frac{d^4I}{dV^4}\right)_{V_o} + \ldots \tag{30}$$

When the AC modulation amplitudes, (A) and (B), are sufficiently small, the amplitudes of the different frequency components of I, divided by their corresponding powers of A and B, converge toward the various differentials of the current-voltage curve. In particular, in the limit $I_{(\omega-\alpha)}$ converges as:

$$\lim_{A,B \to 0} \frac{2}{AB} I_{(\omega-\alpha)} = \left(\frac{d^2 I}{dV^2} \right)_{V_o} \tag{31}$$

where $I_{(\omega-\alpha)}$ represents the amplitude of the output current whose frequency varies at $(\omega-\alpha/2\pi)$ c.p.s., the inter-modulation or "beat" frequency. In measuring the AC beat frequency to determine the second derivatives of the current-voltage curve, it is necessary to apply the convergence criterion as before. That is, successive reductions in A and B should produce reductions in $I_{(\omega-\alpha)}$ proportional to the reduction in the product $(A \times B)$.

In summary, the intermodulation technique is used to measure directly the second derivatives of the current-voltage curve. It is also possible to measure the first derivatives directly by measuring the first harmonics of either fundamental input modulations. However, the first harmonics had superposed on themselves the imperfectly nulled capacitative current mentioned previously. This made accurate direct determination of the first derivatives difficult. Since the second derivatives might be very accurately determined, the first derivatives were obtained by successive integrations of the second derivative. This also eliminated the error which might have been involved in retuning the output wave analyzer at the two different frequencies for each value of DC spectrometer bias.

3. Energy Resolution of AC Measurements

The energy resolution of particle spectrometers is the apparent energy spread given by the spectrometer to monoenergetic particles. The resolution is usually defined as the width at half-height divided by the energy of the line profile of the energy distribution measured for a flux of monoenergetic particles. For the AC technique of measuring the energy spectrum of secondary electrons in the parallel-plate spectrometer, the resolution may be calculated as follows.

Consider first the energy resolution for measurement by the harmonics of a single frequency modulated bias. Let the monoenergetic electron flux be represented by a δ-function,

$$N(V') = \delta(V' - V_1) \tag{32}$$

where V_1 is the energy of the electrons. It was shown in Equation (5) that the net current, $I(V)$, may be expressed as:

$$I(V) = eAR \left[\int_0^V N(V')dV' + \int_V^\infty \left(\frac{V}{V'} \right)^{1/2} N(V')dV' \right] \tag{33}$$

Hence substituting (32) into (33) the current voltage characteristic for monoenergetic electrons is:

$$I(V) = eAR \left(\frac{V}{V_1} \right)^{1/2} \qquad V < V_1 \tag{34}$$

$$I(V) = eAR \qquad V > V_1 \tag{35}$$

The derivatives of I(V) are then:

$$\frac{dI}{dV} = \frac{eAR}{2\,V_1^{\frac{1}{2}}V^{\frac{1}{2}}} \quad , \qquad V < V_1 \tag{36}$$

$$\frac{dI}{dV} = 0 \quad , \qquad V > V_1 \tag{37}$$

$$\frac{d^2I}{dV^2} = -\frac{eAR}{4\,V_1^{\frac{1}{2}}V^{3/2}} \quad , \qquad V < V_1 \tag{38}$$

$$\frac{d^2I}{dV^2} = 0 \quad , \qquad V > V_1 \tag{39}$$

$$\frac{d^2I}{dV^2} = -\frac{eAR}{2V_1}\,\delta(V-V_1) \quad , \qquad V = V_1 \tag{40}$$

These are shown in Figure (2), where $\left(\frac{I}{eAR}\right)$, $\left(\frac{V_1}{eAR}\right)\frac{dI}{dV}$, and $\left(\frac{V_1^2}{eAR}\right)\frac{d^2I}{dV^2}$ are plotted as a function of $\left(\frac{V}{V_1}\right)$.

I(V) may be expressed as a Fourier series:

$$I = \sum_{n=1}^{\infty} A_n \sin n\omega t + B_n \cos n\omega t \quad , \tag{41}$$

UNCLASSIFIED
ORNL-LR-DWG. 37490A

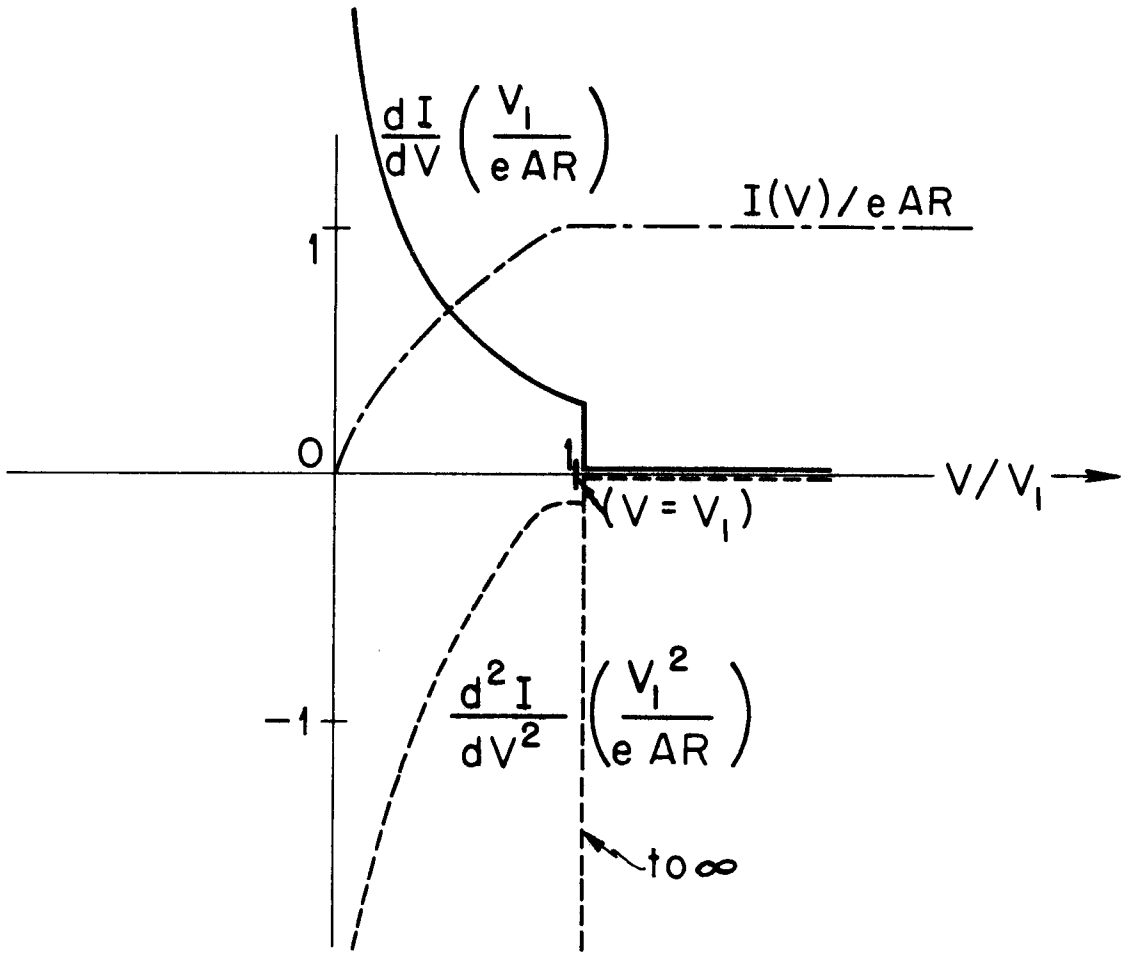

Fig. 2. Current-Voltage Curve and Derivations for Monoenergetic Electrons.

whose coefficients are:

$$A_1 = \frac{1}{\pi} \int_0^{2\pi} I \sin \omega t \, d(\omega t) \tag{42}$$

$$A_2 = \frac{1}{\pi} \int_0^{2\pi} I \sin 2\omega t \, d(\omega t) \tag{43}$$

$$B_1 = \frac{1}{\pi} \int_0^{2\pi} I \cos \omega t \, d(\omega t) \tag{44}$$

$$B_2 = \frac{1}{\pi} \int_0^{2\pi} I \cos 2\omega t \, d(\omega t), \quad \text{etc.} \tag{45}$$

Suppose an AC modulation, a sin ωt, is superimposed on the applied spectrometer bias V_o, where $V_o < V_1$. Define Φ as the phase of the AC at which $V_o + a \sin \omega t = V_1$. Then $\Phi = \sin^{-1} \frac{V_1 - V_o}{a}$ as shown in Figure (3). Evaluating the Fourier coefficient, A_1, from Equations (34) and (42):

$$\frac{A_1 \pi}{eAR} = \int_0^{\Phi} \sqrt{\frac{V_o + a \sin \omega t}{V_1}} \sin \omega t \, d(\omega t) + \int_{\pi-\Phi}^{2\pi} \sqrt{\frac{V_o + a \sin \omega t}{V_1}} \sin \omega t \, d(\omega t) + \int_{\Phi}^{\pi-\Phi} \sin \omega t \, d(\omega t). \tag{46}$$

UNCLASSIFIED
ORNL-LR-DWG. 37491A

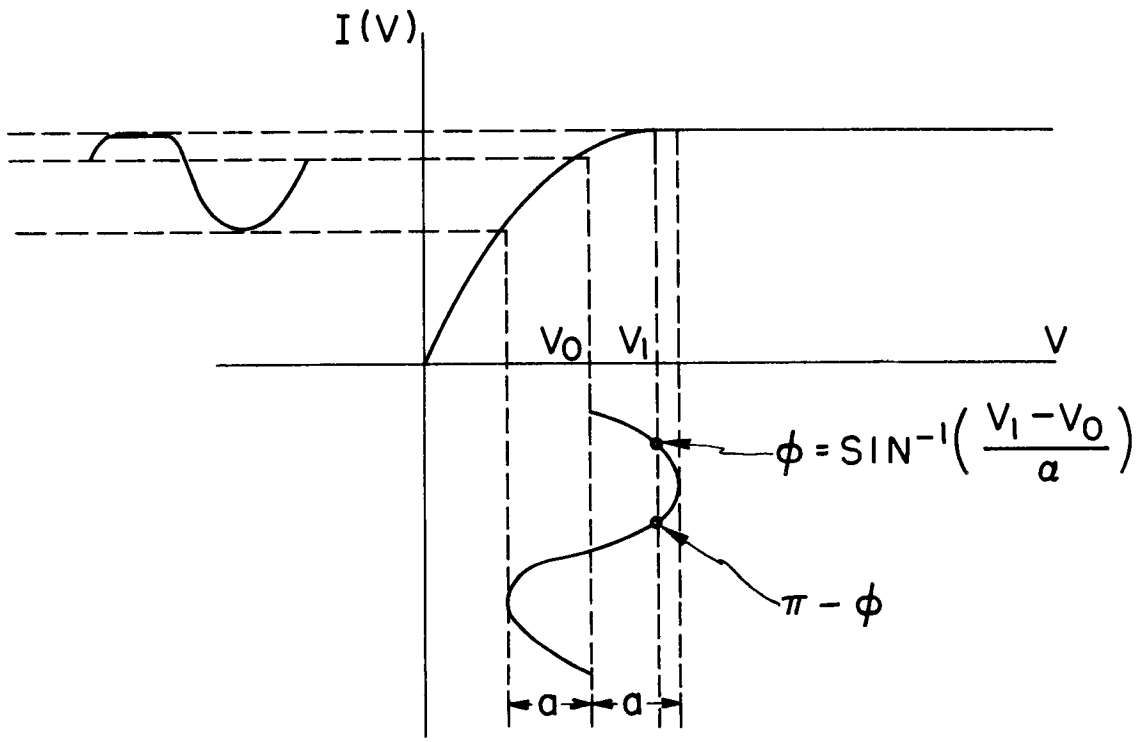

Fig. 3. Phase Angle Analysis for Monoenergetic Electron Line Profile.

By the binomial theorem, $\sqrt{\dfrac{V_o + a \sin \omega t}{V_1}}$ may be approximated by:

$$\sqrt{\frac{V_o}{V_1}} \left(1 + \frac{a}{2V_o} \sin \omega t - \frac{a^2}{8V_o^{\,2}} \sin^2 \omega t \right) .$$

$$\text{Then} \quad A_1 = \frac{eAR}{\pi} \left\{ 2 \cos \phi \left(1 - \sqrt{V_o/V_1} \right) + \frac{a}{\sqrt{V_o V_1}} \left(\frac{\pi}{4} + \frac{\phi}{2} - \sin 2\phi \right) \right. \tag{47}$$

$$\left. - \frac{a^2}{4 V_o \sqrt{V_o V_1}} \left(\cos \phi - \frac{1}{3} \cos^3 \phi \right) \right\} .$$

B_2 may be evaluated similarly from Equations (34) and (45):

$$\frac{B_2 \pi}{eAR} = \int_o^{\phi} \sqrt{\frac{V_o + a \sin \omega t}{V_1}} \cos 2\omega t \, d(\omega t) \tag{48}$$

$$+ \int_{\phi}^{\pi-\phi} \cos 2\omega t \, d(\omega t) + \int_{\pi-\phi}^{2\pi} \sqrt{\frac{V_o + a \sin \omega t}{V_1}} \cos 2\omega t \, d(\omega t) .$$

$$B_2 = \frac{eAR}{\pi} \left\{ 2 \sin \phi \cos \phi \left(\sqrt{V_o/V_1} - 1 \right) + \frac{a}{2\sqrt{V_o V_1}} \left(2 \cos \phi - \frac{4}{3} \cos^3 \phi \right) \right. \tag{49}$$

$$\left. + \frac{a^2}{8 V_o \sqrt{V_o V_1}} \left(\frac{\pi}{4} + \frac{\phi}{2} - \frac{\sin 2\phi}{4} - \sin^3 \phi \cos \phi \right) \right\} .$$

It was shown in Equation (16) that the second harmonic appearing in the output current is in the limit proportional to the second derivative:

$$B_2 \cos 2\omega t = \frac{a^2}{4} \left(\frac{d^2 I}{dV^2} \right)_{V_o} \cos 2\omega t = - I_{2\omega} \cos 2\omega t \tag{50}$$

Hence:

$$\left(\frac{d^2 I}{dV^2} \right)_{V_o} = - \frac{4B_2}{a^2} = - \frac{4}{a^2} \frac{eAR}{\pi} \left[2 \sin \phi \cos \phi \left(\sqrt{V_o/V_1} - 1 \right) + \right.$$

$$\frac{a}{2\sqrt{V_o V_1}} \left(2 \cos \phi - \frac{4}{3} \cos^3 \phi \right) + \frac{a^2}{8V_o \sqrt{V_o V_1}} \left(\frac{\pi}{4} + \frac{\phi}{2} - \frac{\sin 2\phi}{4} \right.$$

$$\left. \left. - \sin^3 \phi \cos \phi \right) \right] . \tag{51}$$

Similarly for the first harmonic Equation (15) showed that in the limit:

$$A_1 \sin \omega t = a \left(\frac{di}{dV} \right)_{V_o} \sin \omega t = I_\omega \sin \omega t \tag{52}$$

Hence:

$$\left(\frac{dI}{dV} \right)_{V_o} = \frac{A_1}{a} = \frac{eAR}{\pi a} \left[2 \cos\phi \left(1 - \sqrt{V_o/V_1} \right) + \frac{a}{\sqrt{V_o V_1}} \left(\frac{\pi}{4} + \frac{\phi}{2} - \frac{\sin 2\phi}{4} \right) \right.$$

$$\left. - \frac{a^2}{4V_o \sqrt{V_o V_1}} \left(\cos \phi - \frac{1}{3} \cos^3 \phi \right) \right] . \tag{53}$$

$N(V_o)$, the flux within the medium may be expressed as:

$$N(V_o) = \frac{1}{eAR}\left[-\left(\frac{dI}{dV}\right)_{V_o} - 2V_o\left(\frac{d^2I}{dV^2}\right)_{V_o} \right] \tag{54}$$

where V_o = DC bias voltage. Hence, for $V_o < V_1$,

$$N(V_o) = -\frac{1}{\pi}\left\{ \frac{2\cos\phi}{a}\left(1 - \sqrt{V_o/V_1}\right) - \frac{a}{4V_o\sqrt{V_oV_1}}\left(\cos\phi - \frac{\cos^3\phi}{3}\right)\right\}$$

$$+ \frac{1}{\pi}\left\{ \frac{16V_o}{a^2}\sin\phi\cos\phi\left(\sqrt{V_o/V_1} - 1\right) + \frac{4V_o}{a\sqrt{V_oV_1}}\left(2\cos\phi - \frac{4}{3}\cos^3\phi\right)\right.$$

$$\left. + \frac{1}{\sqrt{V_oV_1}}\left(-\sin^3\phi\cos\phi\right)\right\} . \tag{55}$$

A similar analysis for $V_o > V_1$, shows that:

$$N(V_o) = -\frac{1}{\pi}\left\{ \frac{2\cos\phi}{a}\left(\sqrt{V_o/V_1} - 1\right) - \frac{a}{4V_o\sqrt{V_oV_1}}\left(\cos\phi - \frac{\cos^3\phi}{3}\right)\right\}$$

$$+ \frac{1}{\pi}\left\{ \frac{8V_o}{a^2}\sin 2\phi\left(1 - \sqrt{V_o/V_1}\right) - \frac{4V_o}{a\sqrt{V_oV_1}}\left(\cos\phi - \frac{\cos^3\phi}{3}\right) + \frac{\sin^3\phi\cos\phi}{\sqrt{V_oV_1}}\right\} . \tag{56}$$

These expressions for $N(V_o)$ may be approximated for $a \ll V_1$

$$N(V_o) = \frac{1}{V_1}\frac{\cos\phi}{\pi}\left\{\frac{-16(V_o/V_1)}{(a/V_1)^2}\sin\phi\left(1 - \sqrt{V_oV_1}\right) + \frac{4\sqrt{V_o/V_1}\left(2 - \frac{4}{3}\cos^2\phi\right)}{a/V_1}\right\}, \tag{57}$$

$$V_o < V_1 \quad ,$$

and

$$N(V_o) = \frac{1}{V_1}\frac{\cos\phi}{\pi}\left\{-\frac{16\ V_o/V_1}{(a/V_1)^2}\sin\phi\left(\sqrt{V_o/V_1} - 1\right) - 4\sqrt{V_o/V_1}\ \frac{\left(2 - \frac{4}{3}\cos^2\phi\right)}{a/V_1}\right\}, \tag{58}$$

$$V_o > V_1 \quad .$$

The graph of this function, Figure (4), shows that the width of the line profile at half-height, the resolution, is:

$$\left(\frac{1.2a}{V_1}\right) \quad \text{or} \quad \left(\frac{1.2a}{V_1}\right) \times 100\ (\%) \quad ,$$

and the base of the line profile is 2a. For the mathematically more complicated analysis of the energy resolution of theintermodulation frequency measurement, it can be argued that the base of the line profile of $N(V_o)$ is no greater than 4a, and that the energy resolution is no greater than:

$$\left(\frac{2.4a}{V_1}\right) \quad \text{or} \quad \left(\frac{2.4a}{V_1}\right) \times 100\ (\%) \quad .$$

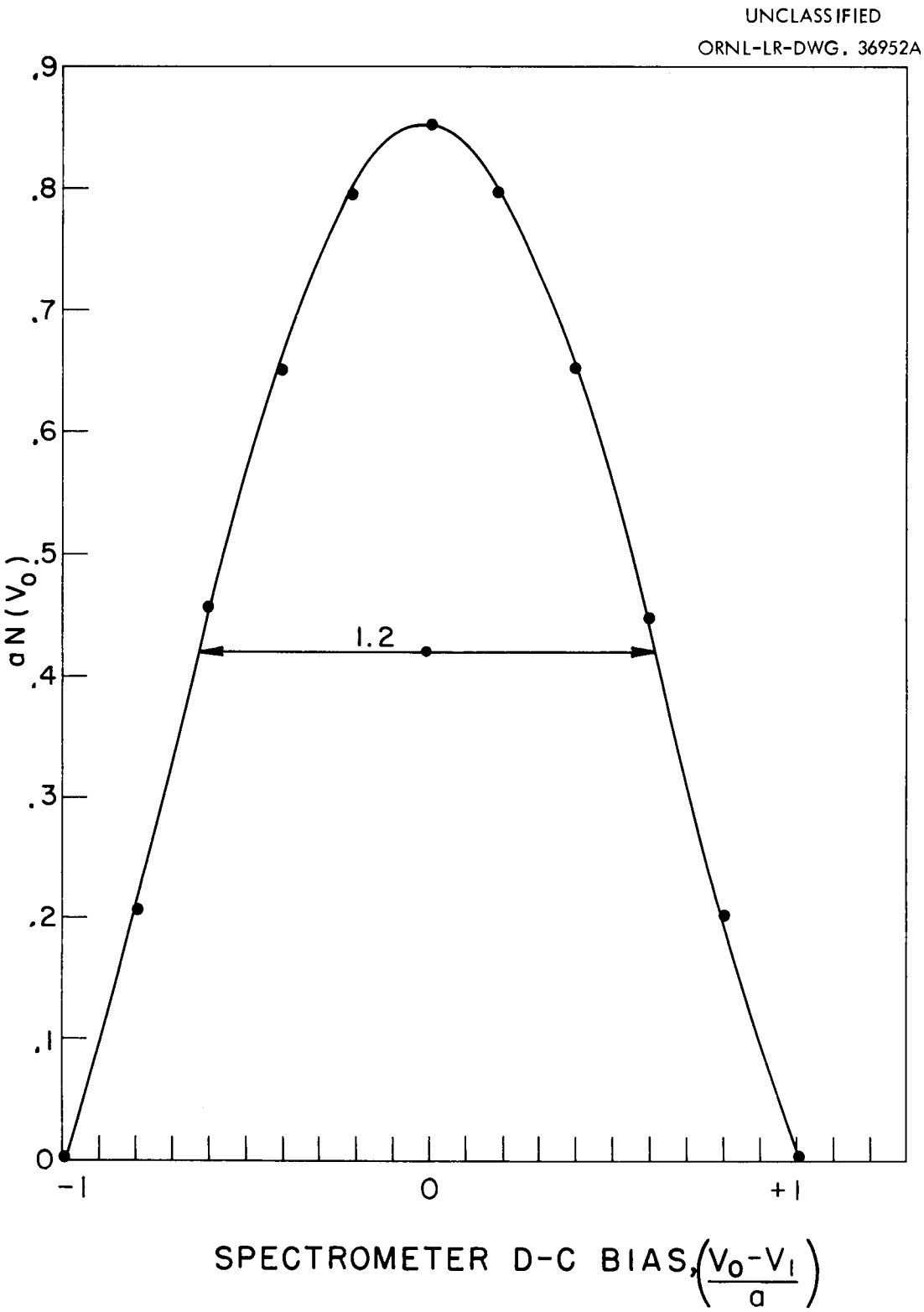

Fig. 4. Line Profile of Parallel-Plate Spectrometer for Monoenergetic Electrons.

III. APPARATUS

A. X-Ray Machine

The X-ray beam was provided by a Westinghouse "Quadrocondex" 250 KVCP machine. The X-ray tube was a Westinghouse WL-395 with an inherent filtration equivalent to 2.5 mm of aluminum. The lid of the vacuum system which housed the spectrometer was fitted with an aluminum cover plate of 2.0 mm thickness. The distance between the target of the X-ray tube and the spectrometer collecting plate was 36 cm. A one-half inch thick lead diaphram with a tapered inside edge, served to define the X-ray beam reaching the spectrometer plates. The X-ray head was placed in position over the vacuum system enclosure, as shown in Figure (5).

The X-ray output was stabilized by controlling the input AC voltage with a Sorenson AC line voltage regulator Model 15000-2S. Erratic fluctuations of as much as 1% existed in the X-ray output. There was a 120 cycle ripple component from the power rectifier of from 2% to 3%. Measurements of the complete spectrum required at most one hour, and the long-term drift during this period was less than 1%.

The X-ray voltages selected for spectral measurements were 180 KVCP and 250 KVCP. Dose rates at lower potentials were not sufficient to produce an accurate measurement of the second derivative. The beam monitoring chamber used by Nelson was eliminated in order to modify the configuration of the test chamber. This modification is described in the following section.

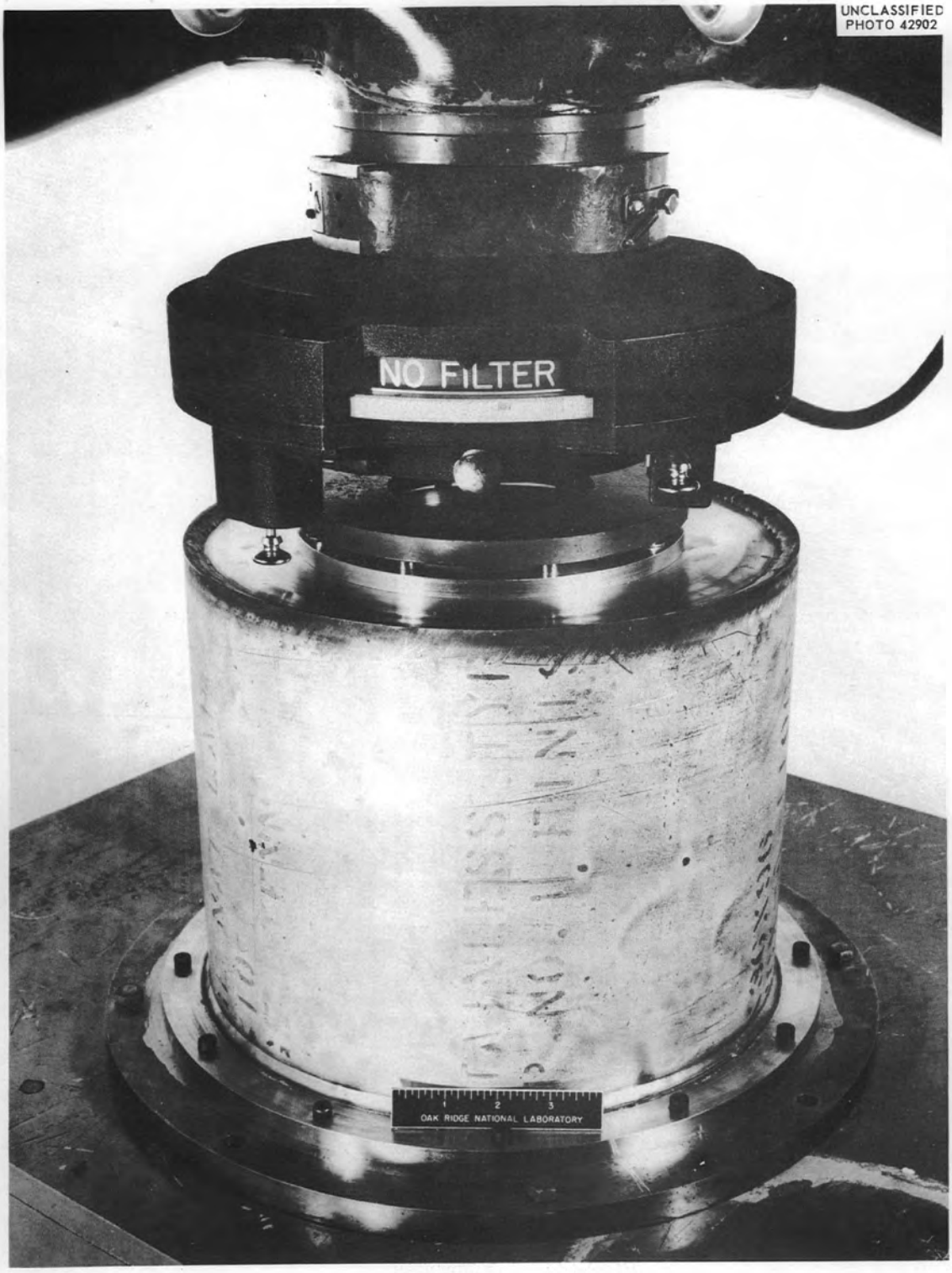

Fig. 5. X-Ray Head and Vacuum System Enclosure.

B. Parallel-Plate Spectrometer

The spectrometer consisted of four plates, as shown in Figure (6). The two outer plates (21.6 cm diameter) supported the inner collecting plates (17.8 cm diameter for copper, aluminum, and graphite; 15.2 cm diameter for conducting tissue equivalent plastic) by means of eight equally spaced fluorothene insulators (3.81 cm long for copper and aluminum, and 1.21 cm for graphite and conducting plastic). The outer plates also served to shield the inner plates from collecting extraneous electrons generated elsewhere in the vacuum system. Electrons were ejected for example from the aluminum cover plate, the vacuum system base plate, and the support rods by the X-ray beam and if collected would add to the true current released from the two central plates of the spectrometer. Since the outer plates were operated at the same potential as the inner plates which they supported, an effective electrostatic shield was attained. The outer plates were supported by aluminum rings (1.27 cm cross-section). H-shaped teflon insulators separated the upper and lower rings. The gap between the collecting electrodes was .635 cm.

To reduce the grid capacitance for the measurement of the spectra in copper and aluminum, the spacing between the lower collecting plate and its supporting plate was increased. The stray capacity to ground had to be minimized in order to attain high impedance at the grid of the pre-amplifier detector. Hence 3.81 cm fluorothene insulators were used in the copper and aluminum measurements. The shorter insulators were used for the other two materials to improve the plate rigidity.

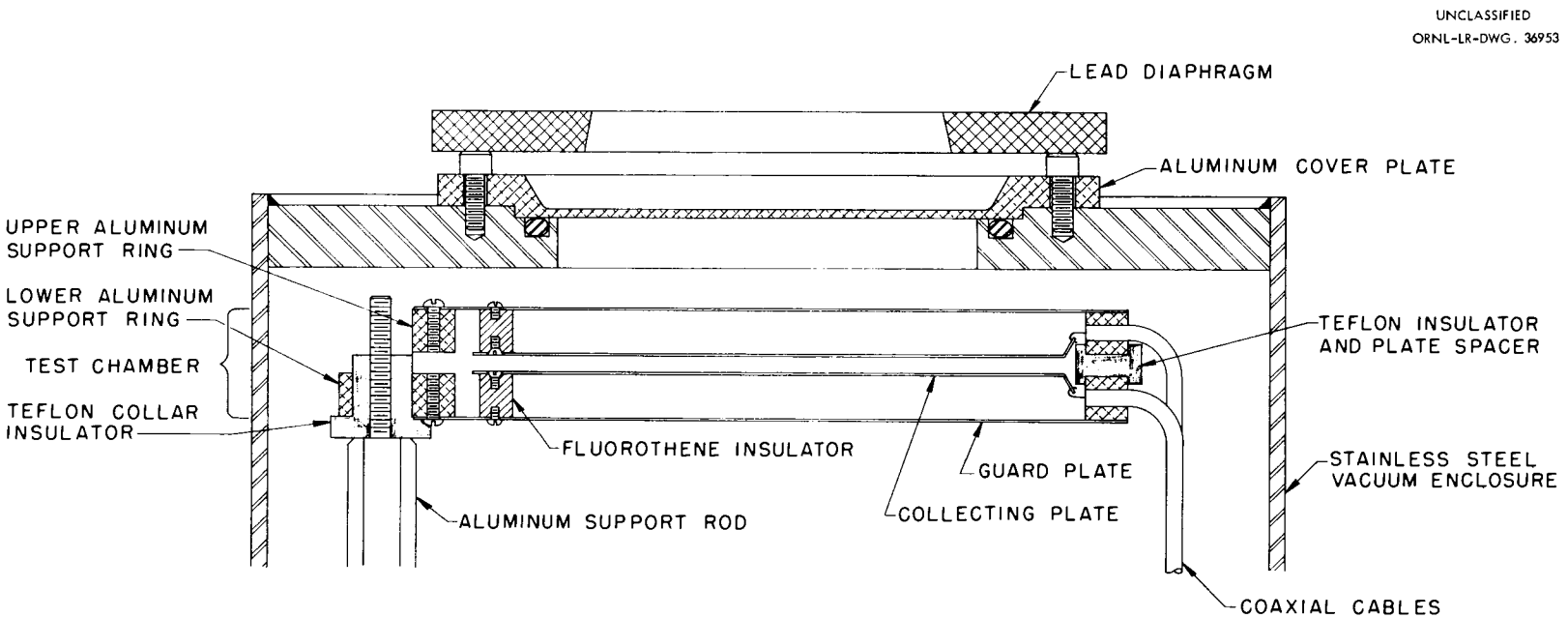

Fig. 6. Parallel-Plate Spectrometer Cross Section.

The plate thickness for each of the materials irradiated was approximately equal to the range of 250 KeV electrons in the material. Theoretical ranges have been given by Spencer[17]. These values and the actual values used in the experimental plates are given in Table I. It is desirable to make the plates approximately equal to the range of the most energetic photoelectron. While the secondary electrons which are actually measured are thought to be generated near the surface of the plate, a plate which was thinner than the range of the primary electrons would not permit the establishment of primary electron equilibrium in the material. A plate thickness which is greater than the range of the primary electrons would attenuate the X-rays unnecessarily.

Table I. Calculations of Spectrometer Plate Thickness

Material	Range g/cm^2	Density g/cm^3	Ideal Thickness (cm)	Thickness (cm)
Copper	.097	8.89	.011	.013
Aluminum	.082	2.669	.030	.033
Graphite*	.079	2.25	.035	.051
Conducting Plastic*	.079	1.06	.074	.074

* The range used was that given for Beryllium, whose atomic number is close to that of graphite and the conducting tissue equivalent plastic.

Measurements of secondary electron yield by Nelson showed that the saturation current yield was dependent on the surface condition of the spectrometer plates. In his measurements, a 20% higher yield was obtained

[17] Spencer, L. V., Phys. Rev. 98, 1597 (1955).

from the chemically cleaned copper than from the annealed copper. The annealing process removes the oxide layer on the copper plates and leaves the surfaces in a condition which is not easily oxidized again. It is interesting to note that the yield from the annealed plates used by Nelson measured one year after annealing was higher by only 10%. A new set of copper plates was annealed in an atmosphere of hydrogen for the new measurements.

The aluminum plates were polished with sapphire dust and cleaned with a detergent and water. The final cleaning of the aluminum was with methyl alcohol and acetone, which were evaporated from the surface in succession. The aluminum oxide layer is formed also instantaneously in air, so no attempt was made to remove it. Graphite and conducting tissue equivalent plastic do not normally exhibit oxides, so no special surface cleaning preparations were taken. The conducting plastic was cleaned with methyl alcohol to remove any surface contaminants.

C. Low Noise Pre-Amplifier

1. General Description of the Circuit

a. Sources of Noise

Amplifier noise affects the accuracy possible in the measurement of low-level signals. The manner in which the noise interferes depends upon the kind of measurement being made. In measuring a sinusoidal current input, the lowest level of detectable signal is approximately equal to the noise level. However, in practice, the unsteadiness of the noise component makes it difficult to measure accurately a signal less than

three times that of the r.m.s. noise. In the present work, AC currents as low as $5 \cdot 10^{-14}$ amp were developed in the vacuum spectrometer. With a practical limit of 10^8 ohm input impedance, it is clear that noise levels, referred to the grid of the pre-amplifier, would have to be on the order of 1 μv from all sources in the grid circuit.

Noise can result from poor engineering and construction: faulty components, hum, microphonics, and electromagnetic and electrostatic pick-up from sources external to the measuring equipment. Another source of noise arises from the fundamental properties of electron current: thermal motion of electrons in the detector load resistor and, grid current, flicker effect, and shot effect in the input tube. If due care is taken in the construction and design of circuit wiring, it can be reliably predicted that one of the latter sources of noise will set the limit on the lowest attainable noise level from an amplifier.

b. Parameters and techniques for reduction of noise due to external sources

Hum

The most obvious source of noise is that arising from 60 cycle AC, its harmonics, and sub-harmonics. This is classified broadly as hum. In the circuit used here, a DC supply for the heater circuits was obtained from a storage cell, placed in a shielded battery box. Similarly, a DC supply for the plate circuit used "B" batteries in a shielded box. Constant voltage transformers while first thought desirable for minimizing line fluctuations in associated AC apparatus, were found to have high leakage fields and hence were not used in the apparatus.

Microphonics

Microphonic noise may have a number of sources: tubes, signal-carrying wires, and the signal source (parallel-plate spectrometer). This noise is due to mechanical vibration. Ruggedized tubes were selected as they are designed to minimize microphonic noise. A most apparent microphonic source in the apparatus was the parallel-plate chamber. Here vibration of the chamber plates produced variation in the chamber's electrical capacitance; hence spurious noise was generated in the signal source itself. The entire apparatus was accordingly shock mounted from the floor to reduce mechanical pick-up of vibrations in the building from fans, compressors, etc. However, a more serious source of microphonic pick-up was found to be the forepump and diffusion pump of the vacuum system associated with the apparatus. A complete description of the techniques used to minimize this noise is given in section E of this chapter.

Relative motion of signal source and detector, as well as cable flexing constitute additional noise sources. To minimize these the pre-amplifier was designed to be placed within the vacuum system. Relative motion of source and detector was reduced, and input signal leads were kept short. Where a longer cable was needed, such as that to the external DC electrometer, a special cable designed to reduce noise arising from cable flexing was used. Variations in the cable capacitance were minimized by an Aquadag coating applied over the dielectric.

In summary, all sources of microphonic noise, mechanical, acoustical, and electrical, were studied. Techniques for reduction were attempted and proved successful.

External Pick-up

Two techniques are commonly used to minimize the pick-up of noise from sources outside the measuring equipment. These are the shielding of cables and high impedance components, and the avoiding of multiple grounds. All cables external to the vacuum system were double conductor, single-shield cables used as shown in the sketch. By grounding the shield at one end only (the source end), noise currents could not be developed along the shield. The pre-amplifier was maintained as the central ground point, and all other equipment grounded only to the pre-amplifier, via the second conductor in the cables. It was recognized that multiple grounds should be avoided because of the possibility that potential differences might exist between them.

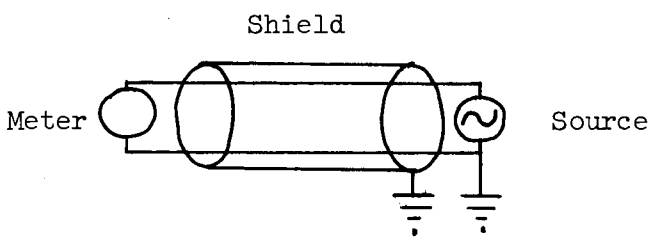

High impedance components are quite sensitive to external electrostatic and electromagnetic fields. Noise pick-up in this case can best be avoided by keeping high impedance leads short and properly shielded. The grid circuit of the pre-amplifier required a high impedance path to ground, $\sim 10^9\ \Omega$. By placing the high resistors near the pre-amplifier input, lead length was kept short. Fortunately, all the high impedance components could be contained

within the vacuum system. The stainless steel vacuum lid and brass base plate constituted an effective electrostatic shield for the circuit. Within the vacuum the input grid components were housed in an aluminum chassis box which provided excellent low-capacity shielding.

The usual trial-and-error method of noise reduction proved valuable in constructing the circuit. The output of the pre-amplifier was monitored with an oscilloscope while various configurations of grounding, shielding, lead-placement, and external equipment were tried. By this method it was possible to reduce the external pick-up to a very low level (0.75 μv at the grid).

c. Parameters and techniques for reduction of inherent noise

Current consists of the movement of charged particles. This movement exhibits statistical fluctuations about a mean value. The fluctuations constitute a noise signal which can be minimized by the choice of circuit and operating conditions. As contrasted to the previously discussed noise sources, this source of noise cannot be completely eliminated.

To consider amplifier noise independently of the input signal is of little value. The parameter of most interest is the signal-to-noise ratio, (S/N). This ratio is a dimensionless number which expresses the ratio of peak signal (volts) to r.m.s. noise (volts). Most of the inherent noise appearing at the grid of the pre-amplifier arises from four sources: first, the high spectrometer load resistor (thermal agitation noise); second, grid-current in the input tube (grid-current noise); third, statistical fluctuations in plate current (shot noise); and fourth, random changes in

cathode emission of the input tube (flicker noise). In selecting a circuit and operating conditions to minimize these sources, the noise signals are assumed to have normal amplitude distribution, and to be independent of each other.

Thermal noise

The random motion of free electrons in the load resistor R of the parallel-plate spectrometer gives rise to a noise voltage which has a mean-square amplitude of

$$\frac{d\bar{v}_t^{\,2}}{df} = 4\,kT_e\,R \tag{59}$$

where $\bar{v}_t^{\,2}$ = mean square thermal noise $(\text{volts})^2$

f = frequency in c.p.s.

k = Boltzmann's constant

T_e = Absolute temperature in °K

R = Chamber load resistance

However, it has been shown by Gillespie[18] that the total noise voltage seen by the amplifier input is expressed as:

$$\bar{v}_t^{\,2} = \frac{k\,T_e}{C_1} \tag{60}$$

[18] Gillespie, A. B., SIGNAL, NOISE AND RESOLUTION IN NUCLEAR COUNTER AMPLIFIERS, (McGraw-Hill Book Co., Inc., 1953) p. 22.

where C_1 = input capacitance. Thus the total thermal noise depends only on the capacitance of the input circuit. This equation gives the upper limit of the thermal noise which may appear at the amplifier input. Hence the size of the grid leak (chamber load) resistor will not appreciably affect the thermal noise appearing at the grid. Later considerations will determine an upper limit on R.

Shot noise

The random variations in mean plate current of a tube give rise to shot noise. For a triode, Schottky[19] showed that

$$\frac{d\overline{v_s}^2}{df} = 4\ kT_e\ \frac{2.5}{g_m} \tag{61}$$

where v_s^2 = mean-square shot noise, g_m = transconductance of the tube, and T_e is assumed to be 290° K.

The similarity of this formula to that for thermal noise should be noted. However, the noise is produced in the electron stream of the tube; hence its amplitude and frequency distribution are independent of the grid input circuit. Shot noise is higher in the pentode because the screen grid reduces the transconductance by drawing off a fraction of the cathode current. Also, since this division in current is subject to random fluctuation, another source of noise, partition noise, appears in pentode operation.

[19] Schottky, W., Ann. Physik 57, 541 (1918).

Grid-current noise

Grid current is a phenomenon observed in all amplifying and receiving vacuum tubes. Random fluctuation in grid current produces a noise signal which is proportional to the absolute magnitude of the current. A number of sources of grid current are known; the parameters which may be adjusted so as to minimize these sources are:

1. Collection of cathode-emitted electrons may be minimized by operating the grid at approximately 2 volts negative with respect to the cathode.
2. Leakage paths over the tube envelope and socket may be minimized by operating in a dry atmosphere, using non-wettable insulators such as teflon, and cleaning the tube and insulators.
3. Collection of positive ions formed when residual gas is ionized by the electron stream can be prevented by operating at low plate potentials.
4. Photoelectrons may be emitted by the control grid under X-rays produced at the plate by the electron stream bombardment. Minimization of this source of current can be obtained by operating the plate at low potentials.
5. Photo-emission from the grid under light, external or cathode, may be minimized by shielding the tube from light and using low heater voltages.
6. Thermionic emission from the grid may be minimized by operating at low cathode temperature.

7. Collection of positive ions emitted by the cathode may also be reduced by low cathode temperature.

8. Collection of radiation-produced ions can be reduced by shielding the grid connection and tube from the radiation field, or eliminated by enclosing the tube in an evacuated container.

In summary, the proper biasing of grid, plate, and cathode, the use of low leakage insulators, operation at low cathode temperature, and light and radiation shielding are techniques for reduction of grid current and its associated noise. The grid current in the input circuit gives rise to a noise signal which can be expressed as

$$\frac{d\overline{v_g}^2}{df} = 2e\,(\Sigma\, I_g)\,\frac{R_1^{\,2}}{1 + \omega^2 T_1^{\,2}} \tag{62}$$

where $T_1 = R_1C_1$ (in ohm-farads), time constant of the input circuit

$\Sigma\, I_g$ = Arithmetic sum of grid current components (amps)

$\overline{v_g}^2$ = Mean-square grid current noise $(\text{volts})^2$.

Flicker noise

Flicker noise is a phenomenon arising in all oxide-coated cathode tubes. Flicker noise is caused by changes in the potential drop across the boundary layer of the oxide-coated cathode. While the reason for the potential variation is not well understood, it is known that the flicker noise referred to the grid is nearly the same for all tubes. While the phenomenon produces

modulation of the cathode current, the noise level is independent of the grid circuit, and the plate current. The spectral density of flicker noise is given by

$$\frac{d\overline{v_f}^2}{df} = \frac{10^{-13}}{f} \tag{63}$$

where $\overline{v_f}^2$ = mean-square flicker noise $(\text{volts})^2$.

d. Selection of Circuit

Signal-to-noise ratio

In the preceding three sections, a consideration of noise sources and parameters of circuitry for noise reduction have been considered. The primary purpose in selecting a circuit is to optimize the signal-to-noise ratio. From the preceding discussion of irremovable noise sources, it can be stated that

$$\frac{S}{N} \;\alpha\; \frac{v_{signal}}{\left[\overline{v_t}^2 + \overline{v_f}^2 + \overline{v_s}^2 + \overline{v_g}^2\right]^{1/2}} \tag{64}$$

It can be shown that thermal noise may be made small with respect to the grid current noise by using a sufficiently high value of grid resistor.

From Equations (59) and (62), the value of R for which the thermal noise becomes equal to the grid-current noise is:

$$R = \frac{2kT_e}{e(\Sigma I_g)} = \frac{5 \times 10^{-2}}{\Sigma I_g} \text{ ohms, at } T_e = 290° \text{ K} \tag{65}$$

In the circuit to be described, it was desired that ΣI_g be kept as low as possible. For a value no greater than 10^{-10} amp, the value of R which would satisfy Equation (65) is $(5 \times 10^{-2})/(10^{-10}) = 5 \times 10^{+8}$ ohms. The lowest value of R was set at 10^9 ohms, thus establishing $\bar{v}_t$ as 25% of $\bar{v}_g$. The upper limit on R will be discussed in a later section.

Furthermore, it was stated that the flicker noise was independent of the operating conditions of the input tube. Optimization of the signal-to-noise ratio is dependent upon only the shot noise and grid current noise. Consideration must then be given to the input circuit, the input tube, and the operating conditions of the input tube.

Operating parameters in tube selection

It was stated in Equation (61) that the spectral distribution of shot noise could be represented as

$$\frac{d\bar{v}_s^2}{df} = 4\,kT_e \frac{2.5}{g_m} \quad \alpha \quad \frac{1}{g_m} \tag{61}$$

Similarly, it was shown that for grid-current noise

$$\frac{d\overline{v_g}^2}{df} = 2e(\Sigma I_g) \frac{R_1^2}{1 + \omega^2 T_1^2} \alpha (\Sigma I_g) \tag{62}$$

A phenomena exhibited by all tubes and circuits is that $g_m \alpha I_K$, i.e., the mutual transconductance is proportional to the cathode current. It is also true that $I_g \alpha I_K$, i.e., the grid current is proportional to the cathode current. The interdependence of shot and grid current noise can then be expressed as

$$\overline{v_s}^2 = k_1 I_k^{-m} \tag{66}$$

$$\overline{v_g}^2 = k_2 I_k^{n} \tag{67}$$

where k_1 and k_2 constants of proportionality, I_K = cathode current, $0 \leq m, \quad n \leq 2$.

Substituting these expressions in (64), Fairstein[20] showed that the conditions which optimize the S/N occur when

$$\frac{v_g^2}{v_s^2} = \frac{m}{n} \tag{68}$$

[20] Fairstein, E., HANDBOOK OF INSTRUMENTS AND TECHNIQUES, (To be published under the sponsorship of the National Research Council Committee on Nuclear Science).

It has been shown that m and n are of the same order for a triode connected tube (with E_{p-g} at the lowest value which allows the grid to be biased more negative than floating-grid potential), when $I_k < 1$ ma. Hence, there is an upper maximum on the cathode current for best signal-to-noise ratio.

Extensive measurements by Fairstein[21] have established that for a typical triode (operated at a grid-bias more negative than floating-grid potential):

1. The grid current is directly proportional to the cathode current.
2. For a given cathode current:

$$I_g = (E_{p-g})^{3/2} \quad I_k \times 10^{-10} \propto (E_{p-g})^{3/2} \tag{69}$$

Hence, in order to maintain low I_g (grid current), it is desirable to operate at as low a plate-grid potential (E_{p-g}) as possible.

For a triode connected tube it is known that

$$I_k = G(E_p + \mu E_g)^{3/2} \tag{70}$$

where G = perveance $\left(\frac{\text{amps}}{\text{volt}^{3/2}}\right)$, μ = amplification factor, E_p = plate-to-cathode voltage, E_g = grid-to-cathode voltage. If an E_g of -1 volt is assumed, then it can be shown that

$$E_p = \left(\frac{I_k}{G}\right)^{2/3} + \mu \tag{71}$$

[21] Fairstein, Rev. Sci. Inst. 29, No. 6, 524 (1958).

Hence, since I_k is limited by previous consideration, the most desirable tubes for low E_p operation are those with low μ and high G (or high g_m). Also, it should be noted that $d\bar{v}_s^{\,2}/df$ shot noise is inversely proportional to g_m. Such a selection of characteristics will also give a tube with low shot noise.

In summary, the characteristics of a low-noise operated tube are:

1. Low μ
2. High g_m
3. Low I_g

} when biased such that { $I_k < 1$ ma, $E_{pk} < 50^v$, $E_{gk} \sim -.5^v$ (with respect to the floating-grid potential)

A number of commercially available tubes exhibiting these characteristics were examined by Fairstein[22]. Among these are the 6AF4, 6T4, 6AJ5, 6AK5, 403B, and 12AF6. Two particularly suitable tubes, 6AJ5 and 6AK5, were selected for the low-noise pre-amplifier used in the experiment. These tubes possessed low I_g ($\sim 10^{-10}$ amp), when operated under the condition specified above.

Circuit Design

Figure (7) shows the circuit of the low-noise pre-amplifier. Basically, the circuit is described as a modified cascode input with a constant-current pentode plate load. The cascode circuit combines advantages found separately in triode and pentode inputs. The middle tube acts as a voltage regulator on the plate of the lower tube, thus increasing the gain of the input stage. The constant-current pentode has the effect of a very large plate resistance, and results in high over-all gain and linearity.

---

[22] Fairstein, E., op. cit.

UNCLASSIFIED
ORNL-LR-DWG. 36956

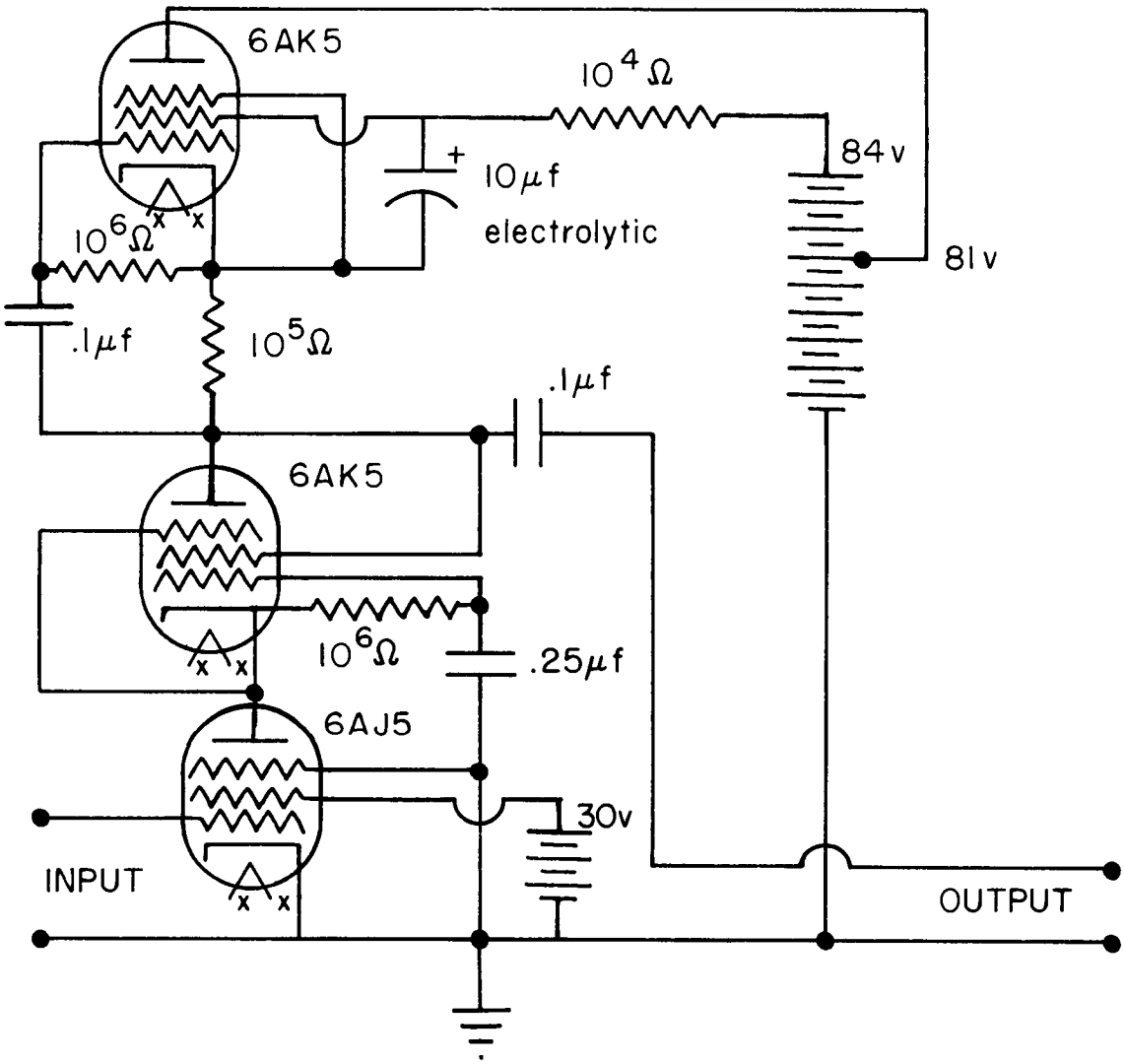

Fig. 7. Low-Noise Pre-amplifier Circuit.

The input tube is operated with a grounded cathode. This gives high voltage gain. Also, the high power gain of this configuration minimizes noise arising in the second stage. The stability is good for small signals. The second tube is operated with grounded grid. This gives high stability. Large input conductance allows the full use of the power gain of the input tube. It should be noted that low plate supply voltage is used, a pre-requisite for low-noise operation. Screen supply voltage for the first tube was built into the amplifier as a small battery, reducing the possibility of external pick-up.

e. Selection of Tubes and Practical Operating Parameters

Tubes

A wide variation in μ, g_m, and inherent noise level is found within tubes of the same type. Therefore, a number of tubes of the type (6AJ5) were selected and each individually checked for gain, grid current, and low noise. Similarly another batch of type 6AK5 was tested and the best individuals selected. Out of approximately fifty tubes ten were selected, and these were rotated to the various positions in the circuit. In this manner it was possible to maxmimize the gain of the pre-amplifier and minimize the noise level for given operating conditions.

Selection of practical operating parameters

At a given value of plate potential and screen potential, a curve of plate current versus grid voltage was taken for each of the fifty tubes. Those exhibiting a region of high gain were selected. The plate current associated

with the region of high gain was of particular interest. The significance of this parameter is as follows:

In part c of this section, grid current noise was discussed. It was pointed out that grid current due to collection of cathode emitted electrons could be minimized by operating the grid at approximately 2 volts negative with respect to the cathode. A graph of grid current-grid voltage for a typical tube is shown in the sketch. The positive I_g portion, to the right of A, represents grid current due to the collection of cathode emitted electrons. The negative I_g portion, to the left of A, represents grid current arising from grid emission, or collection of positive ions. At A, the point of "floating-grid" potential, the various components balance, $\Sigma I_g = 0$. However, it is not here that noise due to grid-current is minimized. The sizes of the individual components to the current each subject to random variation, are not at a minimum. A large component of electron current is here balanced by a large component of ion current. Furthermore, slight fluctuations of the grid bias to the right of A will increase the ΣI_g sharply. In practice the grid is biased approximately .5 volts more negative than A, to the point of maximum negative grid-current. Here, the slope of the curve is zero and slight variation in V_g will

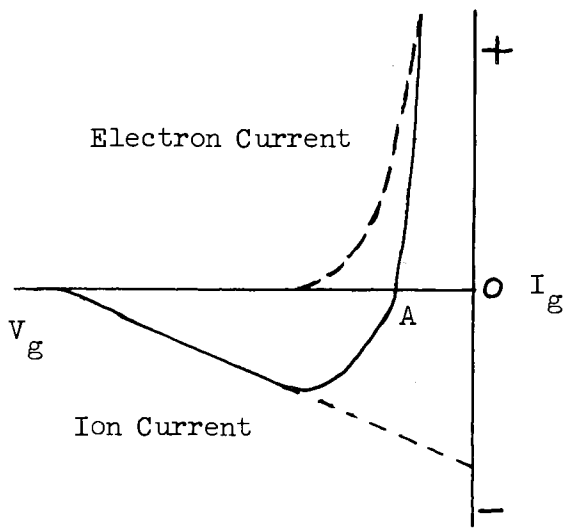

not appreciably alter I_g, and the noise due to electron current will be significantly lower than at A, the floating-grid potential.

The next step in establishing the operating parameters was to determine the floating grid potential and its associated plate current for the high gain tubes selected. Those with floating grid potential such that the associated plate current was less than the plate current of the region of high gain (previously noted), were discarded. It was clear that in order to satisfy the grid bias condition established, it would be necessary for the floating grid plate current to be greater than the plate current in the region of high gain. Of the ten selected tubes, only one exhibited the desired characteristic.

In operating the grid, the grid bias was controlled by the battery on the low end of the grid resistor R_1. By adjusting this potential, it was possible to bias the grid so that the amplifier operated at highest gain and lowest grid-current. Figure (8) shows the graph of I_p versus E_g for the pre-amplifier. The value of E_g associated with $I_{p(max.gain)}$ is approximately one volt more negative than $E_{g(floating)}$. In operation, E_{pk} of the input tube was 12.5^v for $I_K \leq 500$ μa. In this manner the operating conditions best suited for low noise operation were satisified.

2. Construction

a. Electrical

In construction of the electrical circuit of the pre-amplifier, primary consideration was given to minimizing leakage paths, especially in the grid circuit. Teflon tube sockets and hook-up wire with teflon

UNCLASSIFIED
ORNL-LR-DWG. 36957A

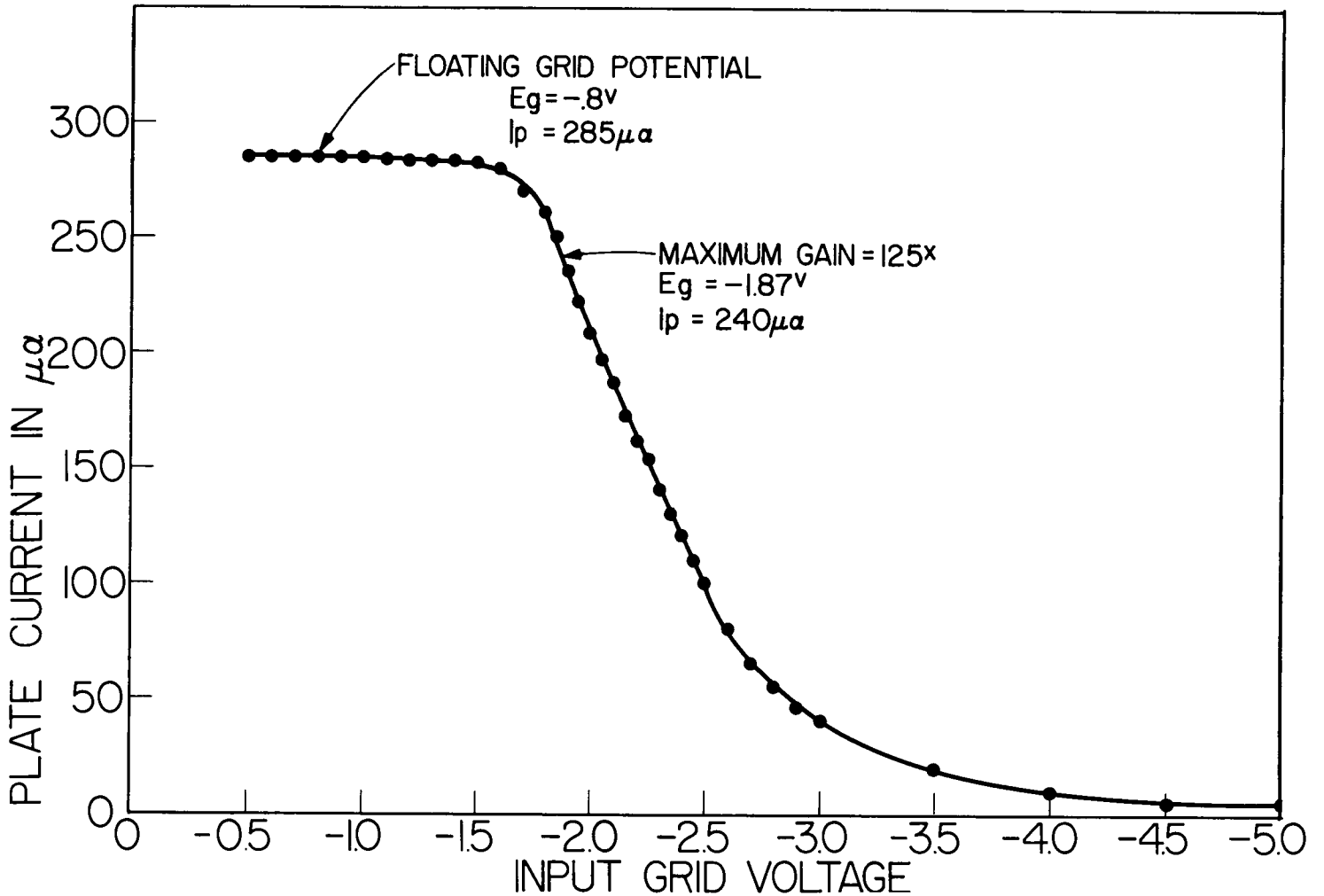

Fig. 8. Plate Current of Output Stage Versus Grid Voltage of Pre-amplifier Input Stage.

insulation were used exclusively. Kovar glass feed-throughs gave high resistance inputs for connections between external leads and internal components. Point-to-point wiring was used within the chassis proper, to conserve space. A single chassis ground point was selected at a location near the input so as to minimize the possibility of ground loops. Sprague "Vitamin Q" capacitors were selected because of low leakage and reduced size. Two 15 volt hearing-aid batteries supplied the screen bias for the input tube.

b. Mechanical

The amplifier was constructed of brass, and consists of three parts: chassis, tube cover, and component cover. The three fit together into an air-tight unit, by means of O-ring seals and bolts. Since the unit has self-contained batteries and an electrolytic capacitor, it was necessary to construct the container air tight so that the pre-amplifier might be contained within the vacuum system. The chassis was fitted with Kovar glass feed-throughs so that access to the electrical components could be made. The brass tube cover also functioned to conduct heat away from the tubes and to shield the tubes electrostatically from the X-ray beam and electric or magnetic fields. A lead disc was placed on top of the amplifier during the measurements to further shield the components from the X-rays. The amplifier is shown in Figure (9), and appears in the photograph of the working apparatus, Figure (10), as it was positioned in the actual measurements.

UNCLASSIFIED
PHOTO 46119

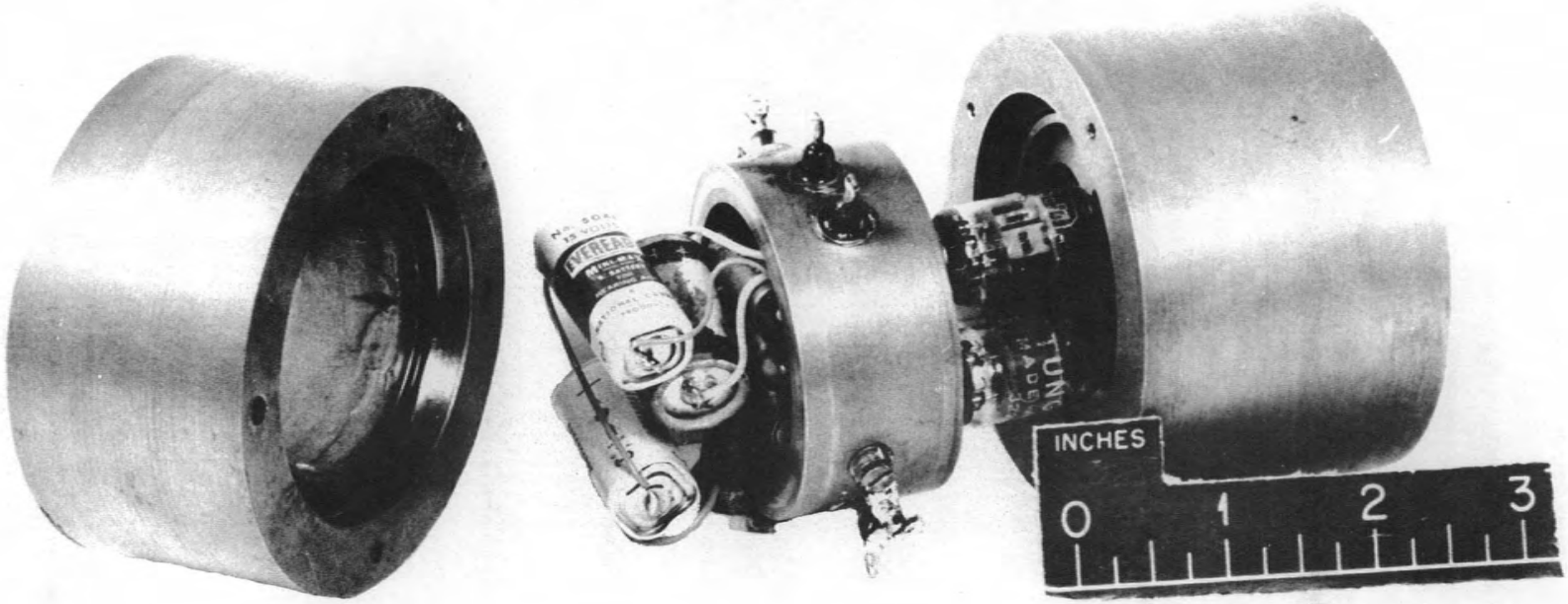

Fig. 9. Low-Noise Pre-amplifier Assembly.

UNCLASSIFIED
PHOTO 46120

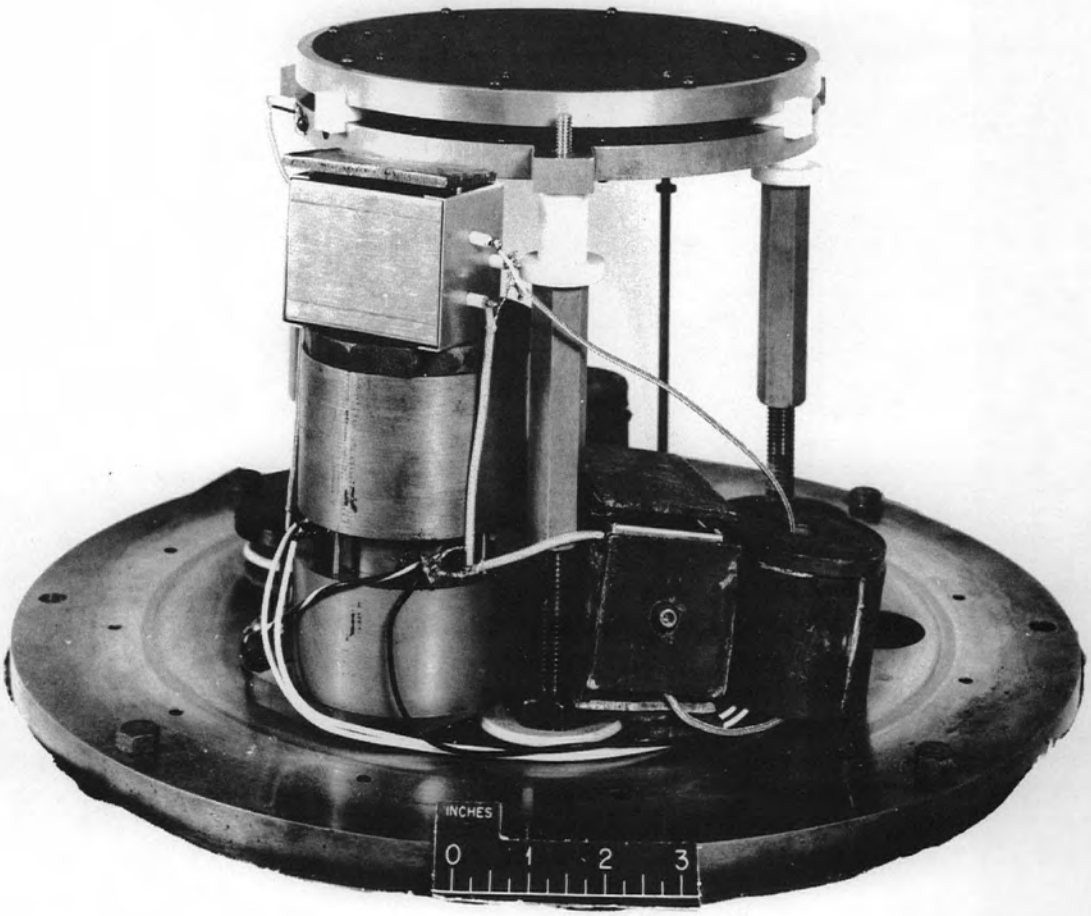

Fig. 10. Parallel-Plate Spectrometer and Pre-amplifier.

D. Electrical Circuit

1. Input

a. Signal generators

Two Hewlett-Packard Model 650-A Test Oscillators supplied the AC bias voltages to the parallel-plate spectrometer. These instruments were selected for their low harmonic distortion and frequency stability. To insure stability the oscillators were operated continuously.

b. Mixing network and balancing circuit

The parallel-plate spectrometer may be represented in the circuit as a capacitance of about 45 μμf. Therefore, AC fundamental voltages if applied directly to the spectrometer plates would be passed to the grid of the pre-amplifier detector. At first thought this might not seem objectionable since the beat frequency resulting from the non-linearity of the current-voltage curve of spectrometer under X-radiation was to be measured, rather than the fundamental frequencies. The passing of the fundamental components to the grid is undesirable, however, since the amplitude of the signals may be of such a magnitude as to over-load the input causing grid rectification and cut-off. For this reason, a null method was devised so that no AC components would appear at the grid of the pre-amplifier when the X-rays were off. When the spectrometer is bombarded by X-rays, a net secondary electron current flows between the plates. The spectrometer then functions with a non-linear current-voltage curve. The DC and AC currents caused by the non-linearity are measured to determine the shape of the current-voltage curve.

The null circuit is shown in Figure (11). The two fundamental AC voltages from the signal generators are applied to the primary winding of the mixing transformer. To prevent the oscillators from loading one another, a simple resistor-capacitor filter was used at the transformer primary. The center tap of the secondary winding of the transformer is grounded for AC through a 1 μf capacitor. The AC voltages developed at the opposite ends of the secondary winding are 180° out of phase. The spectrometer and a variable nulling capacitor are placed in series across the secondary winding. The variable capacitor may then be adjusted so that no AC voltage appears at the grid of the pre-amplifier when the X-ray beam is off. This balance position is attained when the variable capacitance is equal to the capacitance between the spectrometer plates.

The variable nulling capacitor was located within the vacuum chamber in order to minimize the input capacitance and the high impedance lead length. The variable capacitor was enclosed in an aluminum chassis box which was shielded from the X-ray photons by 1/4" of lead on the sides and bottom, and 1/2" of lead on the upper surface. The location of the various components is shown in Figure (10). The input transformer was selected for low distortion and high linearity. It is a General-Radio Type 941-A Toroidal Transformer, connected to give 600Ω primary impedance and 2400Ω secondary impedance. Two matched 40K resistors provided a finite transformer load so that various configurations in the balance

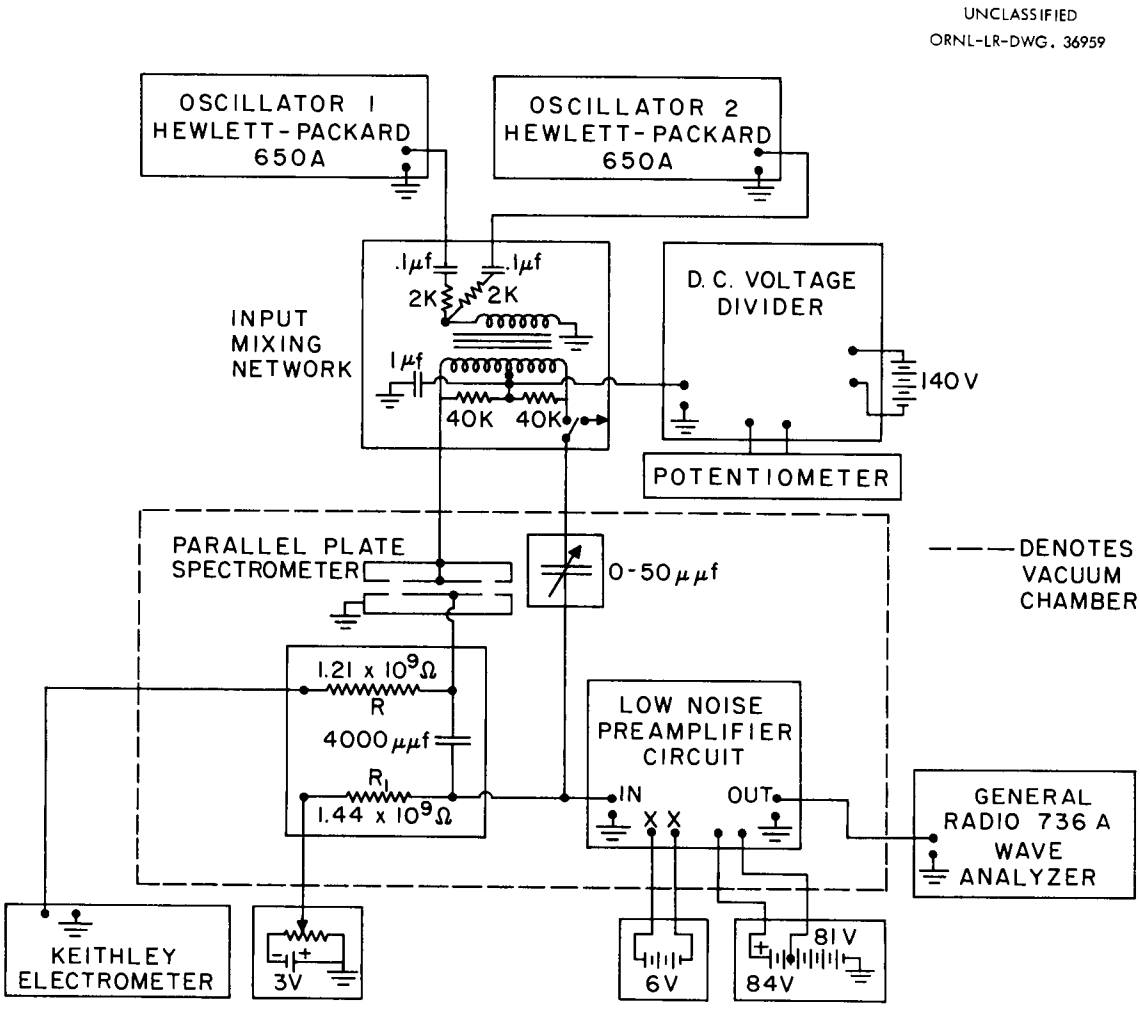

Fig. 11. Circuit Schematic Diagram.

circuit could be used without altering the secondary output of the transformer. DC voltage bias for the spectrometer was applied to the center-tap of the secondary winding of the transformer.

c. Pre-amplifier input network

A resistor-capacitor grid input network was selected so as to isolate the grid from the DC spectrometer current. This prevented variation in DC current in the load resistor, R, from changing the operation bias point of the pre-amplifier. The chamber load resistor and grid resistor were nominally selected at $10^9\Omega$. However, the upper limit of impedance to ground seen by the grid was determined by the capacitance to ground, approximately 45 μμf. At 22 c.p.s. this gave an input impedance of $1.61 \times 10^8\Omega$. The use of $10^9\Omega$ S.S. White resistors represented a compromise between two limits. A lower resistance would have appreciably shunted the capacitative impedance, while a higher value would have increased the time constant of the network to a value on the order of the period of the AC signal measured.

A Fast 4000 μμf blocking capacitor was selected because of its high DC resistance. The body of the capacitor was dipped in ceresin wax in order to improve the surface resistance and to reduce the tendency for outgassing. The DC resistance of the capacitor was higher than $10^{14}\Omega$.

2. Output

a. DC current electrometer

The DC secondary electron current was measured with a Keithley Model 410 Micro-microammeter Serial No. 453. The instrument was connected to

the low impedance end of the 10^9 Ω spectrometer load resistor, R. The electrometer is designed with voltage feed-back so that there is a maximum of 5 mv drop across the input. Hence, the lower end of the load resistor was, in effect, at ground potential at all times. However, the DC spectrometer plate bias had to be corrected for the voltage drop across the 10^9 Ω load resistor.

b. AC Voltage wave analyzer

AC voltages were measured by a General-Radio Type 736-A Wave Analyzer, Serial No. 892. This instrument is essentially a sensitive vacuum-tube voltmeter with a 4-cycle bandwidth. The analyzer was connected to the output of the low-noise pre-amplifier. It was also used to measure the amplitude of the applied AC fundamental modulation.

E. Vacuum System

The vacuum system equipment consisted of a Distillation Products Industries diffusion pump, Model MCF 300-01, a Distillation Products Industries water-cooled baffle, a Welch Manufacturing Company Duo-Seal vacuum forepump, and a Consolidated Electrodynamics Type VST-22 O-ring gate valve. The latter was installed at the entrance to the forepump to seal off (when taking data) the volume into which the diffusion pump exhausted. A General Electric ion gauge supply was used with a Distillation Products Industries VG1A ion gauge to measure the vacuum. The vacuum was maintained at 7×10^{-6} mm of Hg for annealed copper, 5×10^{-6} mm of Hg for aluminum, 5×10^{-6} mm of Hg for graphite, and 8×10^{-6} mm of Hg for the conducting plastic.

The best vacuum was attained when the diffusion pump was operated at 68 volts and 3.80 amperes. This current was low enough to prevent the diffusion pump oil from boiling violently. At currents above 4.00 amperes, the temperature of the oil was high enough to cause random noise pulses to be generated by microphonic vibration of the spectrometer plates.

The vacuum system was designed so that for short periods of time (approximately ten minutes) the forepump could be shut off from the system. The diffusion pump was then allowed to exhaust into the 900 cc volume between the diffusion pump and the forepump. Microphonic noise produced by mecahnical vibration of the spectrometer plates was reduced by this technique. In normal operation when the forepump is on random noise pulses as large as 20 μV at the grid were generated by vibration of the spectrometer plates.

The system could be operated in this manner for twenty minutes or more if necessary. However, as the forepressure in the volume between the diffusion pump and the forepump increased, the pumping speed of the diffusion pump decreased causing a poorer vacuum. A graph of vacuum versus time after forepump is shut off is shown in Figure (12). The vacuum could be returned to its initial value in a few seconds by turning on the forepump and opening the gate valve.

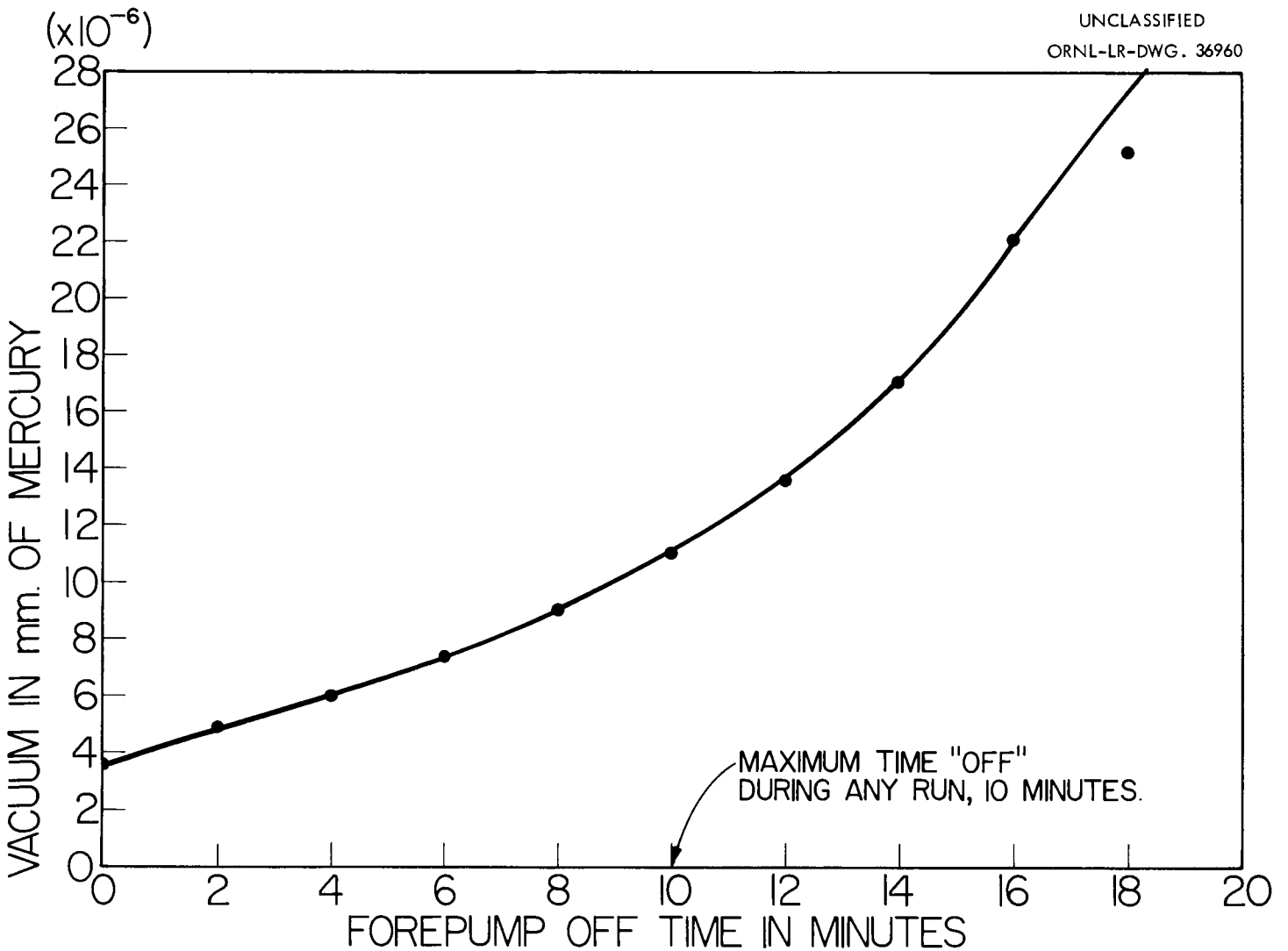

Fig. 12. High Vacuum as a Function of Forepump "Off" Time.

IV. EXPERIMENTAL PROCEDURE AND DATA ANALYSIS

A. Experimental Procedure

Before a set of current-voltage and second derivative-voltage curves were taken, the wave analyzer, oscillators, and electrometer were warmed up for at least two hours. Where such operation was possible, vacuum tube equipment was operated continuously to improve stability and to prolong component life. The first step in the experimental procedure was to calibrate the wave analyzer. Calibration included setting the frequency dials to read correctly, and adjusting the voltage sensitivity to an internally provided 60 c.p.s. calibration signal. The wave analyzer was used throughout the measurements as the AC standard meter. Therefore, the calibration was re-checked frequently during the spectral measurements.

The low noise pre-amplifier was warmed up for about twenty minutes before a run. Then, with no applied AC bias to the spectrometer, the output of the pre-amplifier was scanned with the wave analyzer to determine the frequency region of lowest noise level. At the same time a low frequency region was desirable, since the input impedance of the grid circuit and hence the voltage developed at the grid were inversely proportional to the frequency. It was found for all the measurements that a frequency of 22 to 24 c.p.s. gave the best sensitivity-to-noise ratio. The AC oscillators were tuned to 324 and 300 c.p.s. The initial AC modulation of the spectrometer was set at 100 mv r.m.s. It was found that this value of AC gave sufficient AC beat frequency output so that

an advantageous signal-to-noise ratio could be maintained out to at least 4 volts DC spectrometer bias. Reasonably good energy resolution was to be expected if the AC modulation was less than ten percent of the DC spectrometer bias.

The pre-amplifier plate current was monitored so as to establish the operating conditions of the circuit. By varying the DC potential applied to the low impedance end of the grid resistor, the pre-amplifier could be biased to the operating conditions of highest gain. Plate current was re-checked throughout a run in order to maintain a constant gain in the pre-amplifier circuit.

The X-ray beam was then turned on and the current-voltage and beat frequency-voltage curves were measured. The steep slope of the second-derivative as a function of voltage meant that the amplitude of the output beat frequency declined very rapidly. In order to maintain sufficient intermodulation frequency output, the amplitudes of the fundamental AC signals applied to the spectrometer were increased at regular intervals in the measurement. The fundamental amplitudes were increased in steps of 3x as the output signal decreased in accordance with the decline in the second derivative curve. The measurements were overlapped on the DC bias scale and the amplitude of the AC beat output divided by the square of the AC fundamental input was observed to be a constant, thus satisfying the convergence criterior discussed in Chapter II, Section C-2.

The saturation current (at 30 volts DC bias) was measured for unfiltered and heavily filtered X-rays over the range from 30 KVCP to 250 KVCP. However, the spectral measurements were able to detect a very few secondaries of higher energy than 30 volts for aluminum and copper. The number of such higher energy electrons was so low that the increment which they added to the DC current could not be detected in the most sensitive scale of the electrometer (3×10^{-13} amp). Hence the secondary electron current had reached, in effect, a constant saturation value at 30 volts bias.

Upon completing the spectra and yield measurements for a material, the vacuum system was opened and measurements of the input characteristics of the pre-amplifier were taken. Capacitative impedance to ground was determined with a Tektronix Type 130 LC Meter. The grid resistances were measured on a sensitive bridge circuit. The X-ray flux between the collecting plates of the spectrometer was obtained with a Victoreen Condenser R-Meter, Model 70. For the dose measurements, the geometry during actual operating conditions was duplicated.

B. Data Analysis

The data were analyzed to obtain the energy distribution by calculating the value of the second derivative of the current-voltage curve from the AC beat frequency voltage appearing at the wave analyzer. The energy distribution is largely a function of the second derivative; the first derivative contributes less than ten per cent to the calculated spectra.

The magnitude of the AC current component at the beat frequencies was shown in Chapter II to be related to the amplitudes of the applied AC signals and the second derivative of the current-voltage curve as

$$I_{(\omega-\alpha)} = \frac{AB}{2} \frac{d^2I}{dV^2} \quad . \tag{72}$$

This current develops a voltage at the grid across the input impedance. The voltage amplitude appearing at the wave analyzer is then:

$$E_{output} = \left(\frac{AB}{2}\right) \left(\frac{d^2I}{dV^2}\right) (R) \quad (G) \tag{73}$$

Where R = input impedance, G = amplifier gain, and AB = amplitudes of the fundamental AC modulation.

Solving for $\left(\frac{d^2I}{dV^2}\right)$:

$$\frac{d^2I}{dV^2} = \frac{2}{AB} \frac{E_o}{RG} \left[\frac{amp}{(volts)^2} \right] \tag{74}$$

Considering now the plate area irradiated (a), X-ray dose rate (r), and charge units we find:

$$\frac{d^2I}{dV^2} = \frac{2}{AB} (volts)^{-2} \frac{E_o}{GR} \left(\frac{coul}{sec}\right) \frac{1}{a(cm)^2} \; 3 \times 10^9 \left(\frac{esu}{coul}\right) \frac{1}{r} \left(\frac{roentgen}{sec}\right)^{-1}$$

OR:

$$\frac{d^2I}{dV^2} = \frac{6 \times 10^9 \, E_o}{AB \; R \; ar \; G} \left(\frac{esu}{cm^2 \times r \times volts^2} \right) \tag{75}$$

The first derivatives of the current-voltage curve were calculated by numerical integration of the second derivatives. Assuming that the first derivative is, in effect, zero at energies above that at which the constant DC saturation current is reached:

$$\int_{V'}^{V_{sat}} \frac{d}{dV} \left(\frac{dI}{dV}\right) dV = \left(\frac{dI}{dV}\right)_{V_{saturation}} - \left(\frac{dI}{dV}\right)_{V'} = -\left(\frac{dI}{dV}\right)_{V'} \tag{76}$$

Hence the first derivative at any spectrometer voltage V' may be found by integration of the second derivative from V_{sat} to V':

$$\left(\frac{dI}{dV}\right)_{V'} = \int_{V_{sat}}^{V'} \left(\frac{d^2I}{dV^2}\right) dV \tag{77}$$

The values of $\frac{dI}{dV}$ and $\frac{d^2I}{dV^2}$ were used to calculate the spectra, $eN(E_w + V)$, from Equation (12).

The DC bias voltage on the spectrometer plates was corrected for the voltage drop across the chamber load resistor, R. The DC secondary electron current through this resistor was measured by a Keithley electrometer. This voltage represents the voltage of the lower spectrometer plate with respect to ground. In all cases this was a small correction, less than 0.4 volt.

Calculation of the saturation current density proceeded in a straight-forward fashion. The total current yield was calculated by averaging the yields from measurements with (+) and (-) plate polarity. The saturation current density was then:

$$\bar{I}(V_{sat}) = \bar{I}_{sat} \left(\frac{\text{coul}}{\text{sec}}\right) 3 \times 10^9 \left(\frac{\text{esu}}{\text{coul}}\right) \frac{1}{a(\text{cm})^2} \frac{1}{r\left(\frac{\text{roentgens}}{\text{sec}}\right)}$$

$$= \frac{3\bar{I}_{sat} \times 10^9}{ar} \left(\frac{\text{esu}}{\text{cm}^2 - \text{roentgen}}\right) . \qquad (78)$$

V. EXPERIMENTAL RESULTS

A. Energy Spectra

Figures (13), (14), and (15) show the experimental current-voltage curve, the first, and the second derivatives, respectively for annealed copper. The experimental secondary electron spectra for the four media irradiated are shown in Figures (16), (17), (18), and (19). Two X-ray beam potentials were used, 180 KVCP and 250 KVCP. The beams were unfiltered for these measurements in order to obtain the maximum dose rate. The shape of the energy distributions of the secondary electrons is essentially the same for the two values of incident X-rays. The difference in the magnitudes of the electron distributions, particularly noticeable for aluminum and copper, will be discussed in Section B of this Chapter.

Figures (20), (21), and (22) compare the electron spectra obtained by AC measurements of the second derivatives with Nelson's data, obtained by point-to-point analysis of the DC current-voltage curves. The distributions compare favorably, in the low energy region of Nelson's measurements. Nelson fitted his data with a function:

$$eN(E_w + V) = \frac{\alpha}{(\beta + E_w + V)^2} \tag{79}$$

where α,β = arbitrary constants. The greater sensitivity of the AC technique made it possible to measure the electron flux out to higher values of electron energy. The data shows that for higher electron energies, the distribution falls off more rapidly than the inverse square of the energy. No simple function has been fitted to the data.

UNCLASSIFIED
ORNL-LR-DWG. 36961

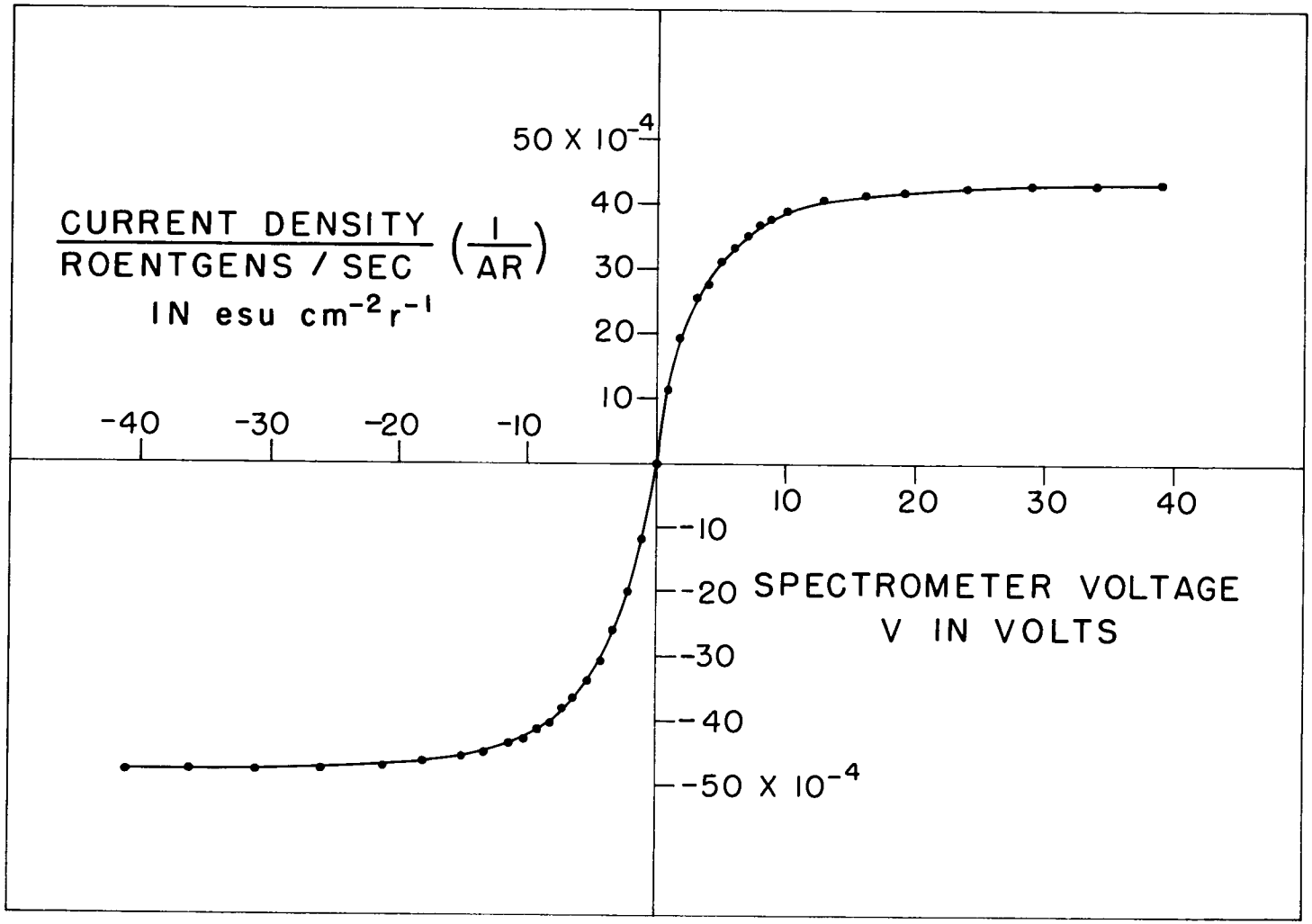

Fig. 13. Current-Voltage Curve for Annealed Copper (250 KVCP X-Rays).

UNCLASSIFIED
ORNL-LR-DWG. 36962

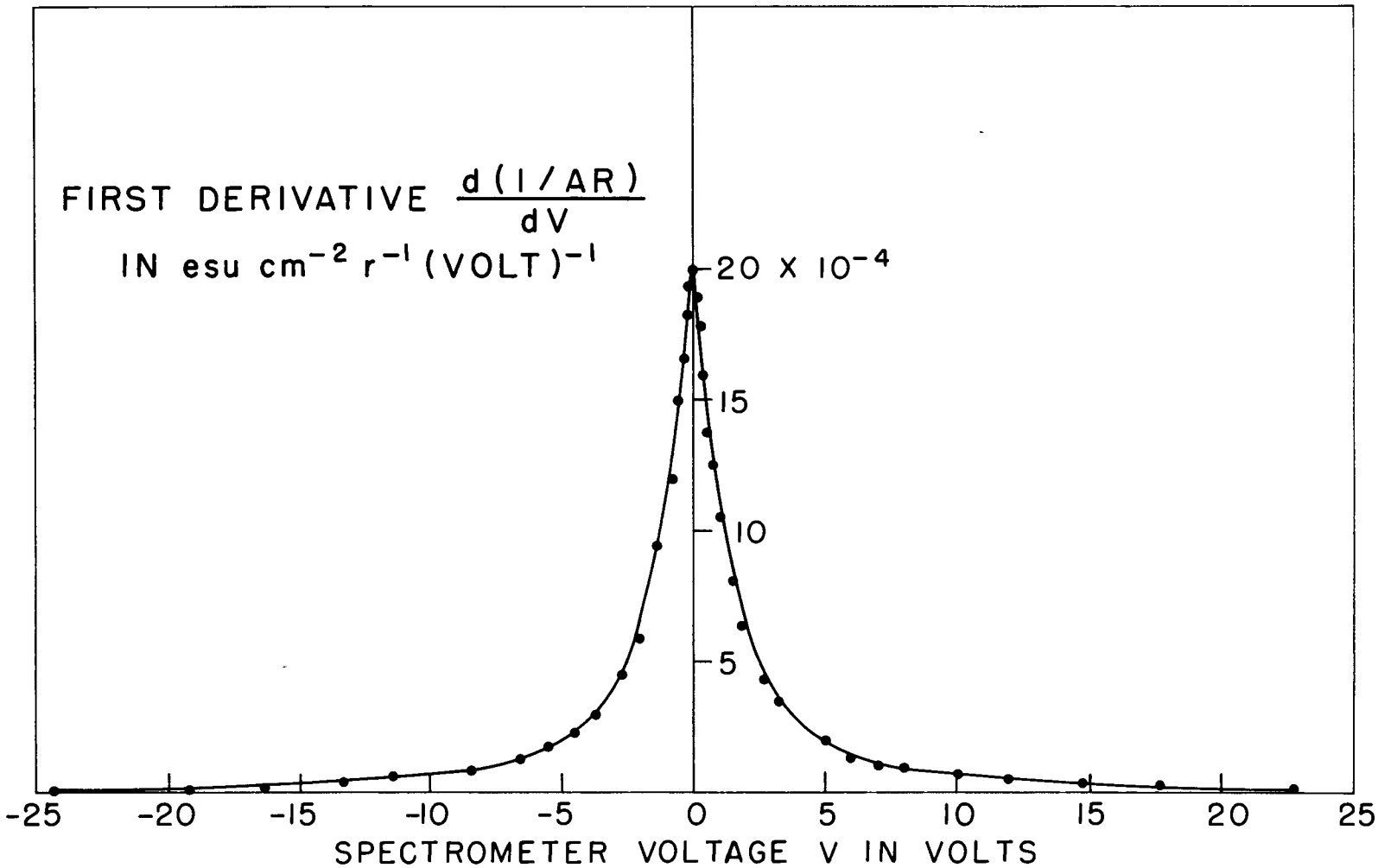

Fig. 14. First Derivative of Current-Voltage Curve for Annealed Copper (250 KVCP X-Rays).

UNCLASSIFIED
ORNL-LR-DWG. 36963

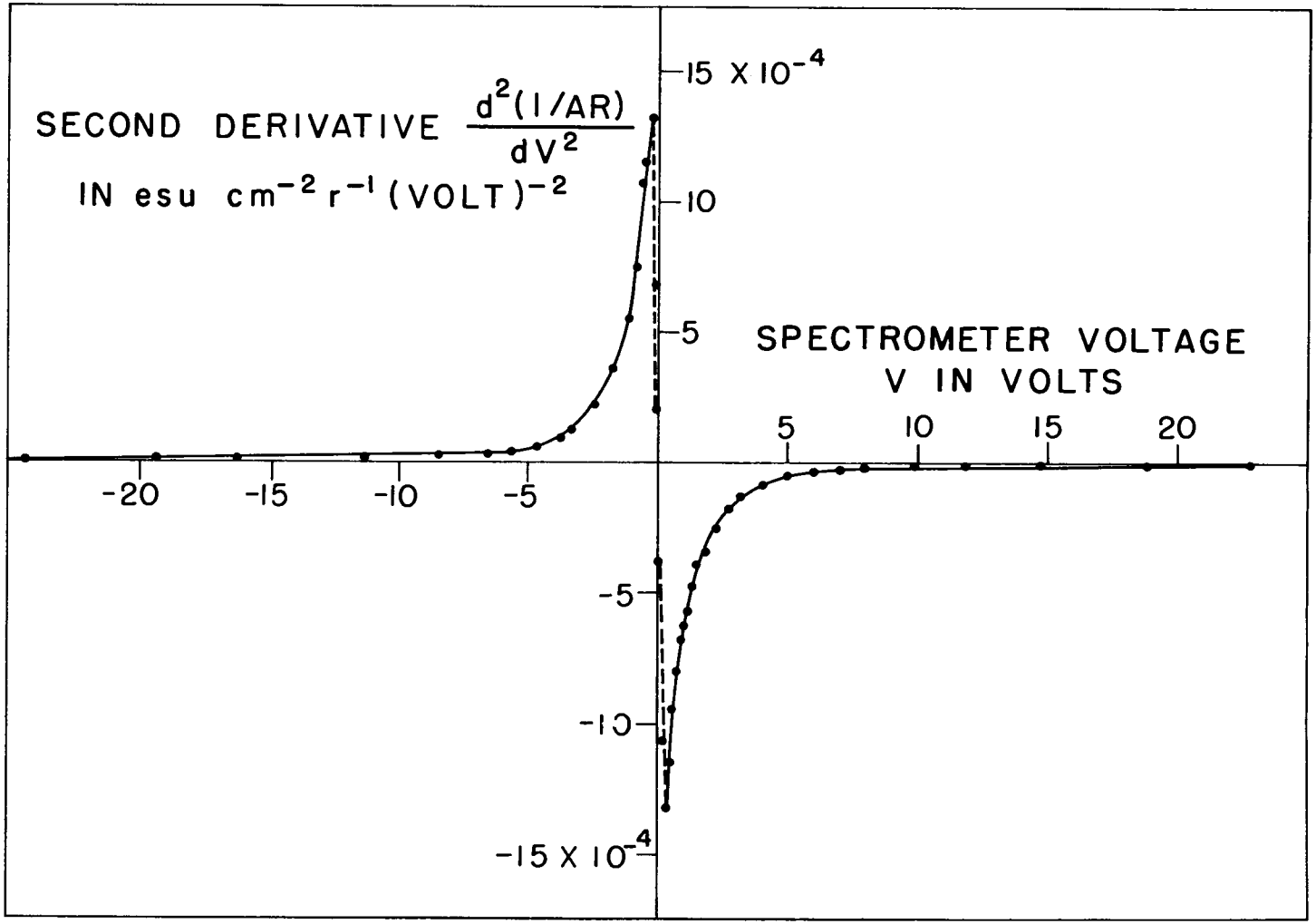

Fig. 15. Second Derivative of Current-Voltage Curve for Annealed Copper (250 KVCP X-Rays).

UNCLASSIFIED
ORNL-LR-DWG. 36964

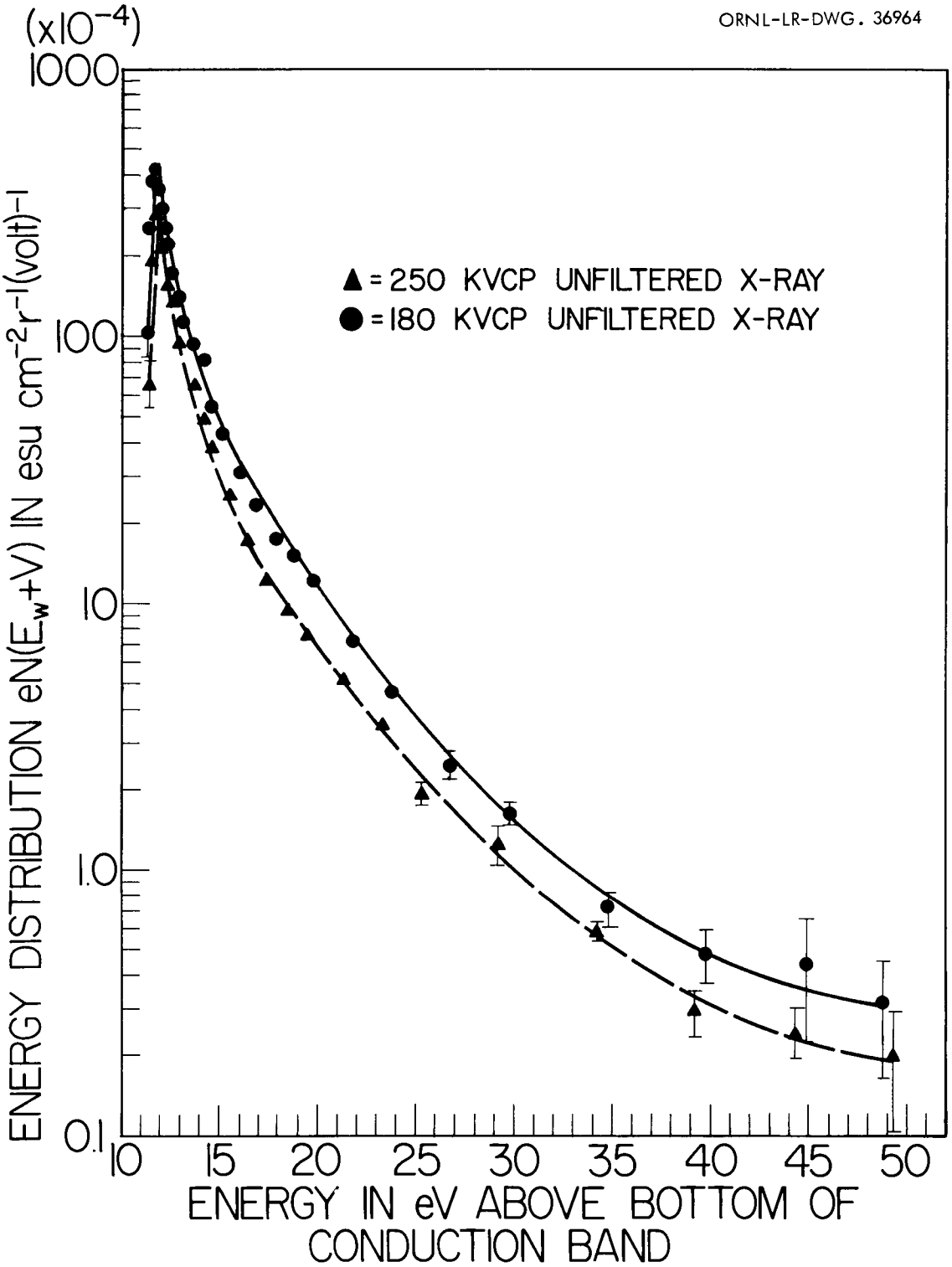

Fig. 16. Energy Distribution of Flux in Annealed Copper.

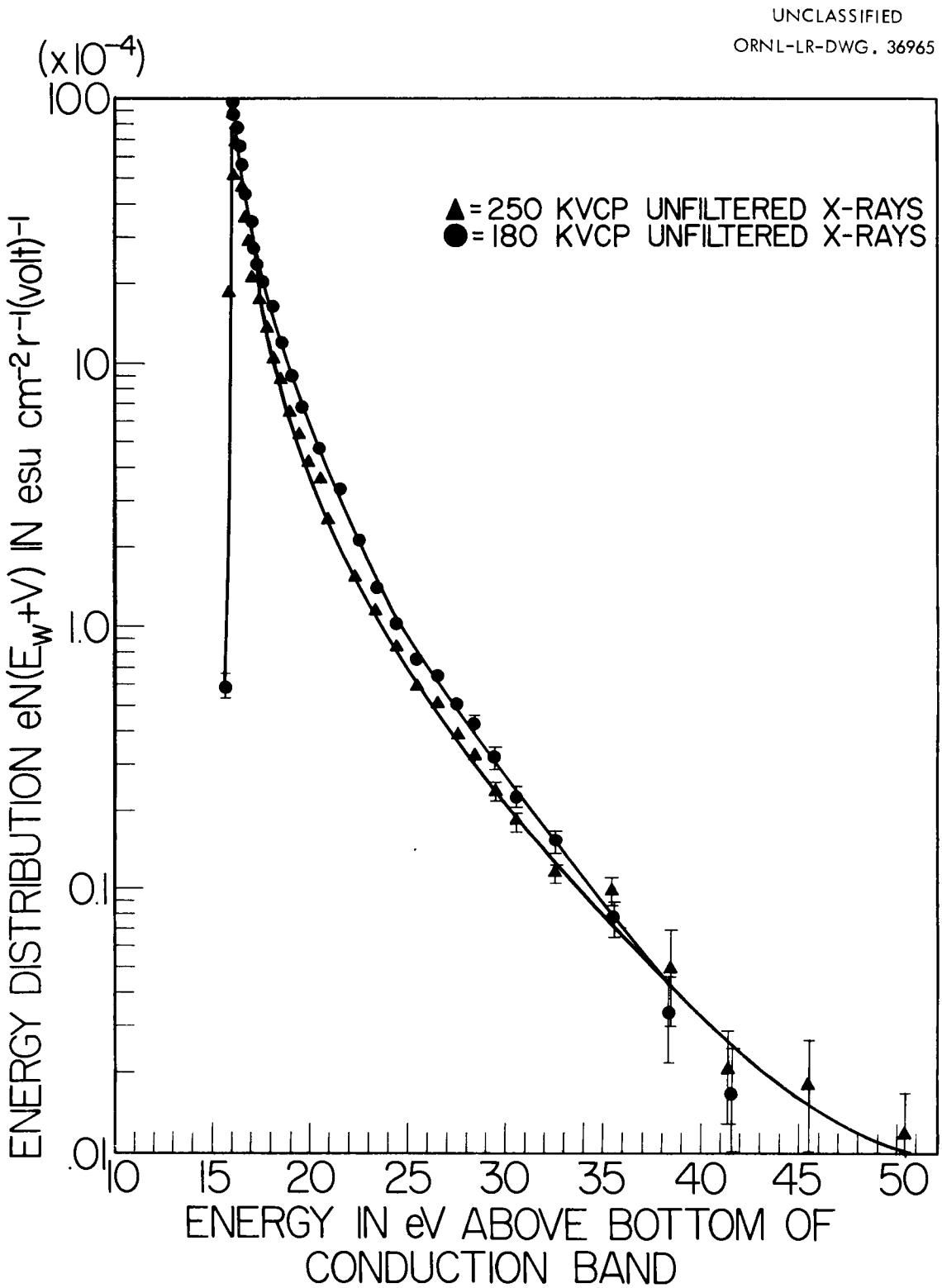

Fig. 17. Energy Distribution of Flux in Aluminum.

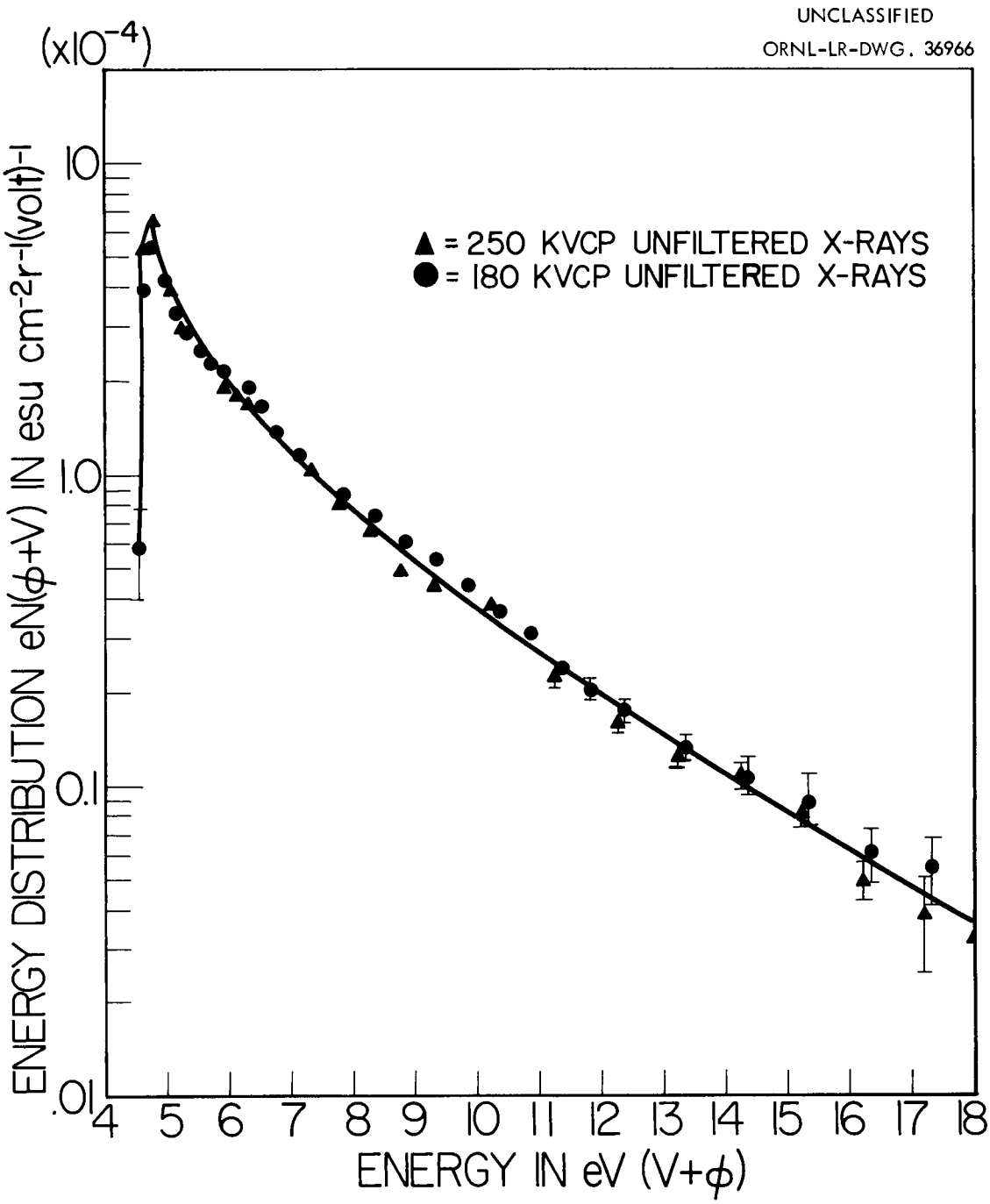

Fig. 18. Energy Distribution of Flux in Graphite.

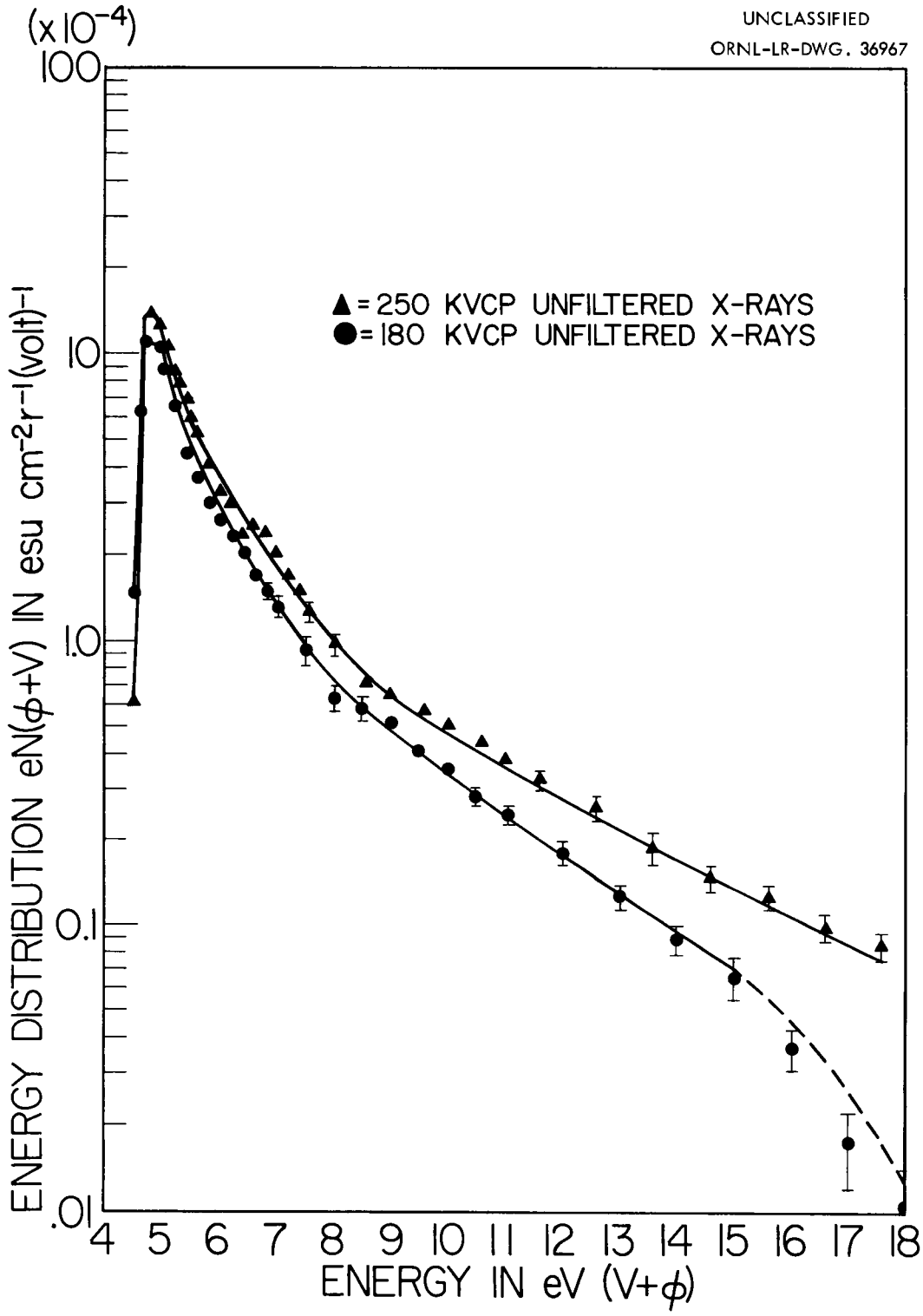

Fig. 19. Energy Distribution of Flux in Tissue Equivalent Conducting Plastic.

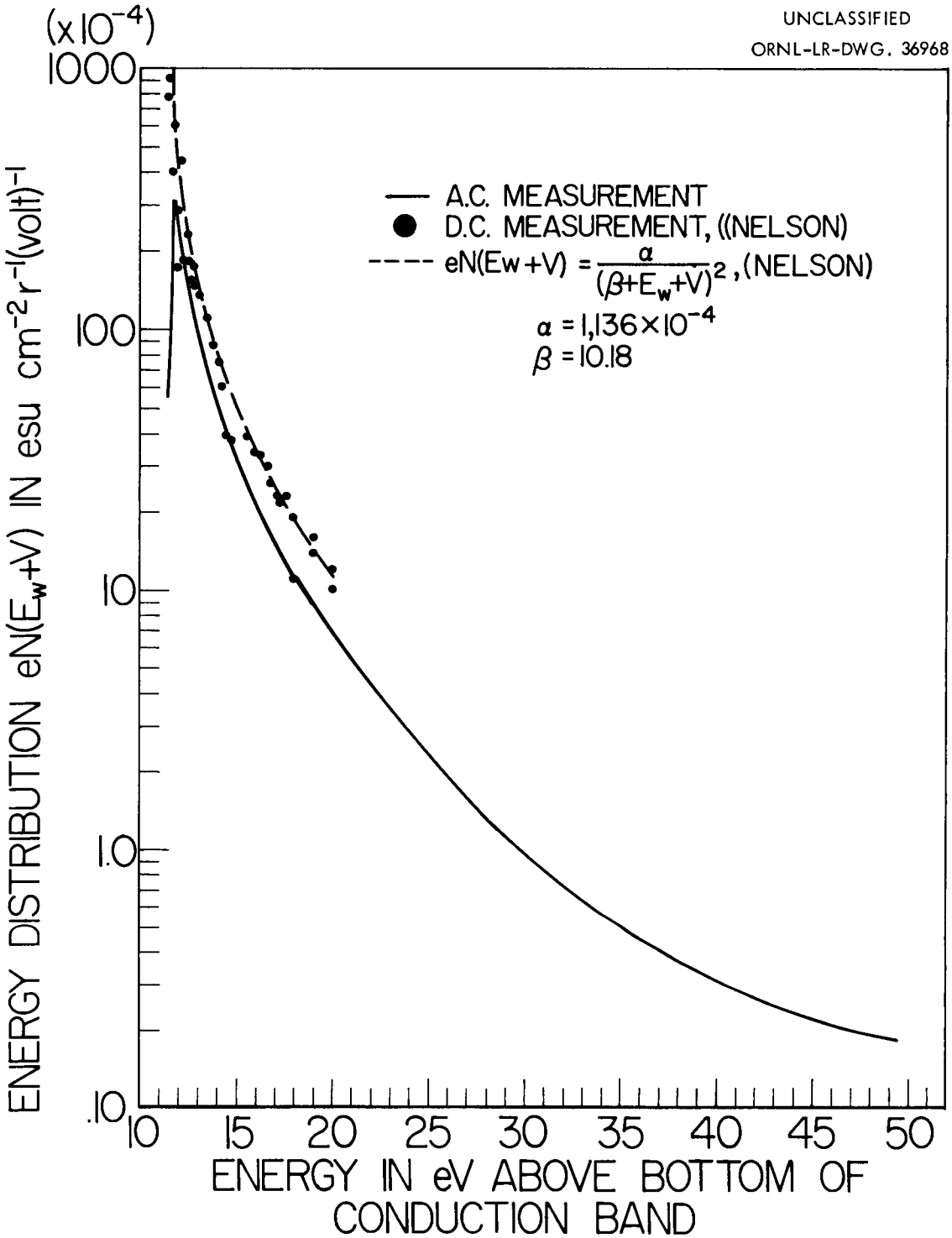

Fig. 20. Comparison of Energy Distribution for Annealed Copper (250 KVCP X-Rays) with Nelson's Data.

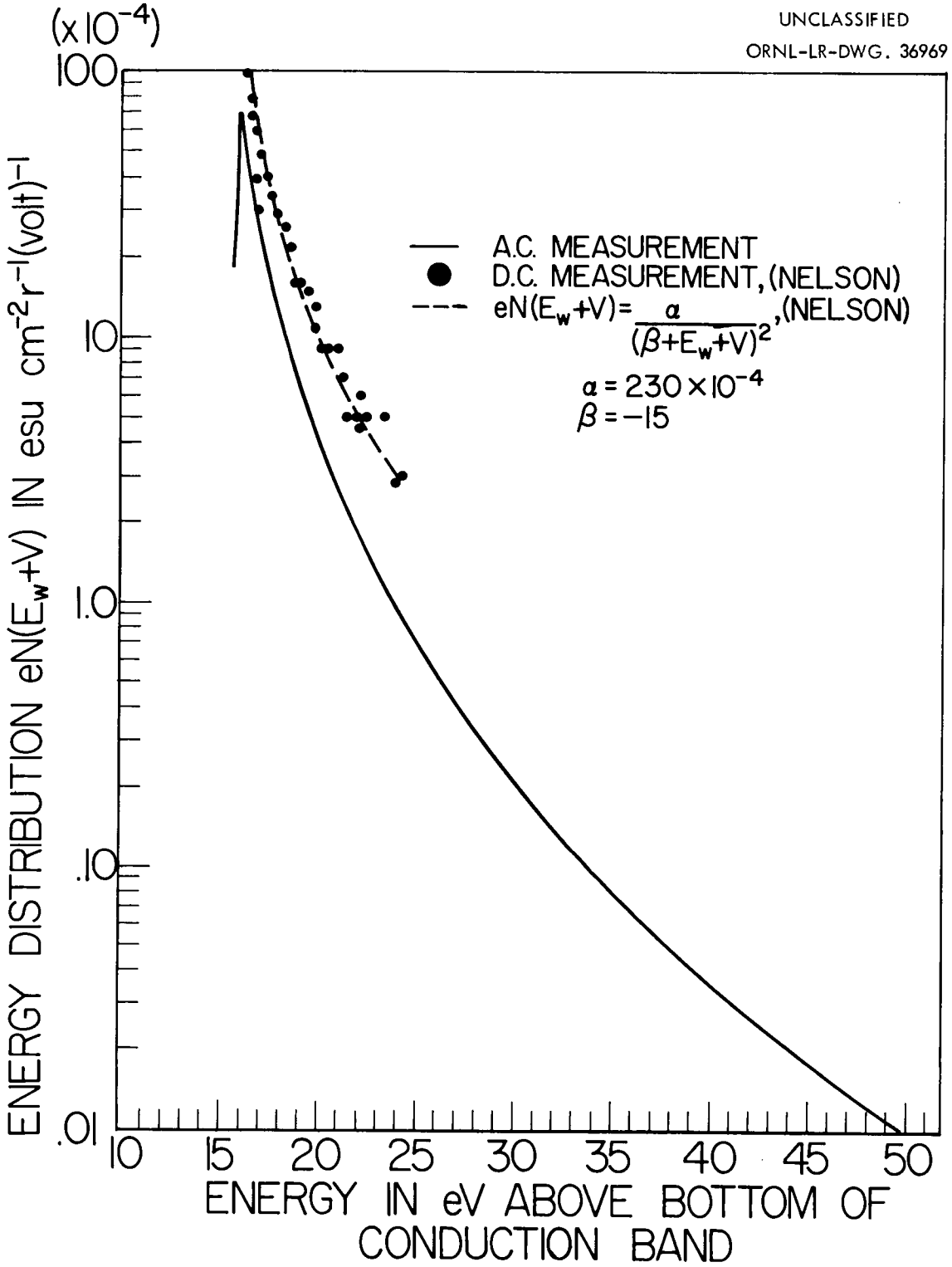

Fig. 21. Comparison of Energy Distribution for Aluminum (250 KVCP X-Rays) with Nelson's Data.

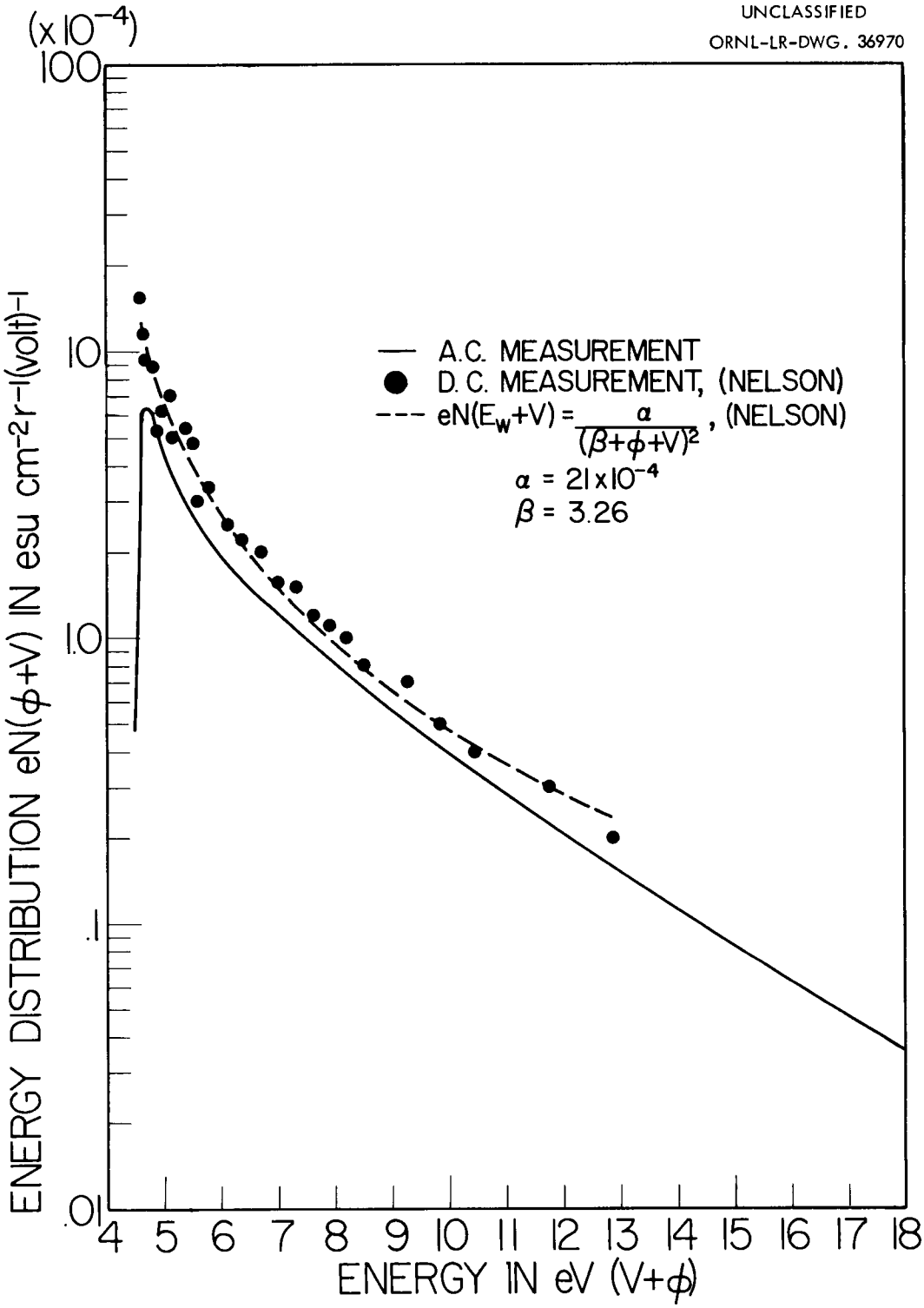

Fig. 22. Comparison of Energy Distribution for Graphite (250 KVCP X-Rays) with Nelson's Data.

The discrepancy in the magnitudes of the energy distributions obtained by the AC and DC methods is caused primarily by differences in the cleanness of the plates of the spectrometer. Nelson discovered that the thicker the oxide layer on the copper plates, for example, the high was the total yield of electrons. The variation in the condition of the plate surfaces resulted in a saturation current yield which was ten per cent lower for graphite and aluminum, and thirty per cent lower for copper in the present measurements. This information, applied to the electron flux spectra as a normalization factor, would bring the energy distribution curves into better agreement. Tables II, III, IV and V list the energy distributions numerically.

B. Saturation Current Density

The DC current from the parallel-plate spectrometer is very nearly constant above 25 volts DC bias. Taylor[23] and Nelson have made measurements of the current density at saturation for various media. Nelson's measurements were made with unfiltered X-rays and may be compared with data taken in this experiment (Table VI, columns two and three). Taylor's measurements were taken for heavily filtered X-rays and may be compared for data taken with heavily filtered X-rays in this experiment (Table VI, columns four and five). The saturation current density is given in $\frac{\text{esu}}{\text{cm}^2 \text{ - roentgen}}$.

[23] Taylor, L. S., op. cit.

Table II. Energy Distribution in Annealed Copper

250 KVCP X-Ray (Unfiltered)		180 KVCP X-Ray (Unfiltered)	
V (Volts)	$eN(E_w + V)$ $\left(\frac{esu}{cm^2 r(Volt)}\right)$	V (Volts)	$eN(E_w + V)$ $\left(\frac{esu}{cm^2 r(Volt)}\right)$
.04	.0068	.03	.0104
.10	.0193	.10	.0256
.16	.0229	.16	.0383
.23	.0276	.23	.0422
.29	.0291	.29	.0416
.35	.0284	.37	.0406
.41	.0270	.43	.0365
.47	.0258	.50	.0333
.53	.0229	.57	.0302
.60	.0217	.64	.0284
.67	.0203	.72	.0256
.74	.0185	.79	.0243
.89	.0156	.87	.0221
1.03	.0146	.94	.0208
1.19	.0137	1.01	.0191
1.35	.0114	1.17	.0172
1.50	.0095	1.33	.0157
1.93	.0073	1.50	.0141
2.30	.0066	1.68	.0131
2.76	.0049	1.85	.0113
3.23	.0039	2.27	.0095
4.12	.0025	2.72	.0082
5.05	.0018	3.17	.0055
5.99	.0012	3.63	.0044
6.94	.00094	4.57	.0031
7.89	.00076	5.51	.0024
9.84	.00051	6.47	.0017
11.80	.00035	7.43	.0015
14.76	.00019	8.41	.0012
17.76	.00012	10.40	.00072
22.75	.00006	12.34	.00047
27.72	.00003	15.33	.00025
32.72	.00002	18.31	.00016
		23.30	.00007
		28.30	.00005
		33.30	.00004
		38.30	.00003

Table III. Energy Distribution in Aluminum

250 KVCP X-Ray (Unfiltered)		180 KVCP X-Ray (Unfiltered)	
V (Volts)	$eN(E_w + V)$ $\left(\frac{esu}{cm^2 r(Volt)}\right)$	V (Volts)	$eN(E_w + V)$ $\left(\frac{esu}{cm^2 r(Volt)}\right)$
.06	.00189	0	.00006
.14	.00518	.08	.0054
.22	.00694	.17	.0089
.30	.00649	.25	.0096
.38	.00593	.34	.0089
.47	.00524	.43	.0078
.55	.00467	.51	.0067
.64	.00383	.60	.0058
.73	.00348	.69	.0050
.91	.00291	.78	.0044
1.09	.00212	.96	.0035
1.26	.00183	1.15	.0028
1.44	.00173	1.33	.0024
1.63	.00156	1.52	.0022
1.82	.00139	1.71	.0020
2.00	.00118	2.18	.0017
2.19	.00105	2.66	.0012
2.38	.00096	3.14	.00090
2.57	.00087	3.63	.00068
3.06	.00065	4.61	.00049
3.54	.00053	5.60	.00034
4.02	.00042	6.59	.00021
4.51	.000367	7.58	.00014
5.49	.000253	8.58	.00010
6.48	.000156	9.57	.000076
7.47	.000117	10.57	.000064
8.47	.000085	11.57	.000052
9.46	.000061	12.57	.000043
10.46	.000052	13.57	.000032
11.46	.000040	14.57	.000023
12.46	.000032	16.57	.000015
13.46	.000024	19.57	.000008
14.46	.000019	22.56	.0000068
16.45	.000012	25.56	.0000035
19.45	.000010	28.56	.0000019
22.44	.000005	31.56	.0000004
25.44	.000002		
29.44	.0000018		
34.44	.0000013		
39.44	.0000006		

Table IV. Energy Distribution in Graphite

250 KVCP X-Ray		180 KVCP X-Ray	
V (Volts)	$eN(E_w + V)$ $\left(\frac{esu}{cm^2\ r\ (volt)}\right)$	V (Volts)	$eN(E_w + V)$ $\left(\frac{esu}{cm^2\ r\ (volt)}\right)$
0	.000024	0	.00006
.09	.00054	.10	.00039
.19	.00066	.20	.00054
.28	.00055	.29	.00047
.38	.00045	.39	.00042
.47	.00039	.49	.00037
.57	.00033	.58	.00033
.66	.00030	.68	.00029
.76	.00028	.78	.00028
.95	.00025	.98	.00026
1.15	.00023	1.17	.00023
1.35	.00019	1.37	.00022
1.54	.00018	1.57	.00021
1.74	.000172	1.78	.00019
2.23	.000142	1.98	.00017
2.72	.000103	2.18	.000138
3.22	.000080	2.38	.000126
3.71	.000067	2.58	.000116
4.21	.000050	2.78	.000113
4.71	.000044	3.29	.000087
5.70	.000038	3.79	.000074
6.70	.000023	4.29	.000062
7.70	.0000162	4.80	.000054
8.69	.0000126	5.30	.000044
9.69	.0000109	5.80	.000036
10.69	.0000072	6.30	.000032
11.69	.0000051	6.80	.000024
12.69	.0000039	7.30	.000021
13.69	.0000031	7.80	.0000175
		8.30	.0000151
		8.80	.0000132
		9.81	.0000108
		10.81	.0000089
		11.81	.0000062
		12.81	.0000055

Table V. Energy Distribution in Tissue Equivalent Conducting Plastic

250 KVCP X-Ray (Unfiltered)		180 KVCP X-Ray (Unfiltered)	
V (Volts)	$eN(E_w + V)$ $\left(\frac{esu}{cm^2\ r\ volt}\right)$	V (Volts)	$eN(E_w + V)$ $\left(\frac{esu}{cm^2\ r\ volt}\right)$
0	.00006	0	.00015
.09	.00104	.10	.00062
.19	.00138	.19	.00110
.29	.00141	.29	.00109
.38	.00127	.39	.00104
.48	.00116	.49	.00089
.57	.00103	.68	.00066
.67	.00088	.88	.00045
.77	.00079	1.08	.00037
.87	.00070	1.27	.00030
.96	.00060	1.47	.00026
1.06	.00053	1.67	.00023
1.26	.00041	1.87	.00021
1.46	.00033	2.07	.00017
1.65	.00030	2.27	.00015
1.85	.00024	2.47	.00013
2.05	.00026	2.97	.000093
2.25	.00024	3.46	.000063
2.44	.00020	3.96	.000058
2.64	.00017	4.46	.000052
2.84	.00015	4.96	.000042
3.04	.00013	5.46	.000035
3.53	.000097	5.96	.000028
4.03	.000071	6.46	.000024
4.53	.000065	7.46	.000018
5.03	.000057	8.46	.000013
5.53	.000052	9.46	.0000089
6.03	.000044	10.45	.0000076
6.53	.000038	11.45	.0000038
7.02	.000033	12.45	.0000017
8.02	.000026	13.45	.0000011
9.02	.000019		
10.02	.000015		
11.02	.0000128		
12.02	.0000099		
13.02	.0000088		
14.02	.0000073		
15.02	.0000038		
16.02	.0000016		
17.02	.0000011		

Table VI. Current Densities at Saturation

Medium	X-Ray KVCP	Unfiltered X-Ray Nelson	Experimental Unfiltered X-Ray	Heavily Filtered X-Ray; Taylor[24]*	Experimental Heavily Filtered X-Ray**	Experimental Heavily Filtered X-Ray (rad dose)***
		esu $cm^{-2}r^{-1}$	esu $cm^{-2}r^{-1}$	esu $cm^{-2}r^{-1}$	esu $cm^{-2}r^{-1}$	esu $cm^{-2}(rad)^{-1}$
Aluminum	250	1.1×10^{-3}	1.0×10^{-3}	$.26 \times 10^{-3}$	$.41 \times 10^{-3}$	$.48 \times 10^{-3}$
	200		1.1×10^{-3}	$.32 \times 10^{-3}$	$.47 \times 10^{-3}$	$.52 \times 10^{-3}$
	150		1.3×10^{-3}	$.42 \times 10^{-3}$	$.61 \times 10^{-3}$	$.51 \times 10^{-3}$
	100		1.9×10^{-3}	$.81 \times 10^{-3}$	1.25×10^{-3}	$.49 \times 10^{-3}$
	76		1.9×10^{-3}		1.69×10^{-3}	$.47 \times 10^{-3}$
	50		1.9×10^{-3}		2.25×10^{-3}	$.47 \times 10^{-3}$
Graphite	250	$.24 \times 10^{-3}$	$.21 \times 10^{-3}$	$.23 \times 10^{-3}$ *	$.31 \times 10^{-3}$	$.37 \times 10^{-3}$
	200		$.22 \times 10^{-3}$	$.24 \times 10^{-3}$ *	$.30 \times 10^{-3}$	$.39 \times 10^{-3}$
	150		$.22 \times 10^{-3}$	$.27 \times 10^{-3}$ *	$.31 \times 10^{-3}$	$.37 \times 10^{-3}$
	100		$.21 \times 10^{-3}$	$.26 \times 10^{-3}$ *	$.26 \times 10^{-3}$	$.37 \times 10^{-3}$
	76		$.19 \times 10^{-3}$		$.22 \times 10^{-3}$	$.40 \times 10^{-3}$
	50		$.17 \times 10^{-3}$		$.21 \times 10^{-3}$	$.48 \times 10^{-3}$
Annealed Copper	250	6.3×10^{-3}	4.4×10^{-3}		$.67 \times 10^{-3}$	$.36 \times 10^{-3}$
	200		4.9×10^{-3}		1.05×10^{-3}	$.36 \times 10^{-3}$
	150		6.7×10^{-3}		2.44×10^{-3}	$.31 \times 10^{-3}$
	100		8.4×10^{-3}		6.79×10^{-3}	$.22 \times 10^{-3}$
	76		9.3×10^{-3}		9.28×10^{-3}	$.20 \times 10^{-3}$
	50		7.0×10^{-3}		8.55×10^{-3}	$.15 \times 10^{-3}$

Continued

Table VI. Current Densities at Saturation Continued

Medium	X-Ray KVCP	Unfiltered X-Ray Nelson	Experimental Unfiltered X-Ray	Heavily Filtered X-Ray; Taylor[24]*	Experimental Heavily Filtered X-Ray**	Experimental Heavily Filtered X-Ray (rad dose)***
Tissue-Equivalent Conducting Plastic ****	250		$.29 \times 10^{-3}$		$.35 \times 10^{-3}$	$.40 \times 10^{-3}$
	200		$.28 \times 10^{-3}$		$.39 \times 10^{-3}$	$.44 \times 10^{-3}$
	150		$.28 \times 10^{-3}$		$.38 \times 10^{-3}$	$.42 \times 10^{-3}$
	100		$.25 \times 10^{-3}$		$.33 \times 10^{-3}$	$.43 \times 10^{-3}$
	76		$.24 \times 10^{-3}$		$.32 \times 10^{-3}$	$.55 \times 10^{-3}$
	50		$.22 \times 10^{-3}$		$.28 \times 10^{-3}$	$.61 \times 10^{-3}$

* Figures for graphite-coated bakelite.

** Effective X-ray energies for experimental data from heavily filtered beam:

KVCP	KeV Effective
250 KVCP	(201 KeV)
200 KVCP	(159 KeV)
150 KVCP	(114 KeV)
100 KVCP	(68 KeV)
76 KVCP	(45 KeV)
50 KVCP	(35 KeV)

*** Absorbed dose calculated from the relation:

$$J_{saturation}\left(\frac{esu}{cm^2\text{-}r}\right) \times \frac{(\tau+\sigma_\alpha+K_T)_{air}}{(\tau+\sigma_\alpha+K_T)_{med.}} \times \frac{100(r)}{83(rad)} = J_{sat}\left(\frac{esu}{cm^2\text{-}rad}\right)$$

(25)

**** Tissue-equivalent conducting plastic made by Markite Corp., New York, N. Y. By weight: C = 82%, H = 10.4%, O = 4.1%, and N = 3.5%.

[24] Taylor, L. S., op. cit.

[25] Storm, E., Gilbert, E., Israel, H., "Gamma-Ray Absorption Coefficients ... ", LA-2237, Los Alamos Scientific Laboratory, Los Alamos, New Mexico (1958).

For the heavily filtered X-rays the saturation current density for copper and aluminum shows a higher yield per roentgen at low photon energies than at high photon energies. The yield per roentgen was fairly constant for graphite and tissue equivalent plastic. This phenomena suggests a correlation between the saturation current and the mass absorption coefficients of the media. Column six of Table VI lists the saturation current density in $\frac{\text{esu}}{\text{cm}^2\ \text{rad}}$, i.e., as a function of the dose absorbed in the media. The yield per rad is relatively constant for the photon energies from 45 KeV to 200 KeV. Also, the absolute yield per rad is very similar for the four media considered. The saturation current densities are plotted as a function of incident dose and absorbed dose in Figures (23) and (24) respectively. It is difficult to determine accurately the effective mass absorption coefficient for the low energy photon spectra. The error in the determination of this coefficient is believed to be the cause of the apparent decline in the yield per rad for copper at low incident photon energy.

The physical picture which explains the above may be hypothesized as follows: incident photons produce primary Compton and photoelectrons in the medium (a plate of a thickness which is sufficient to give electron equilibrium). The low energy secondary electrons measured in the parallel-plate spectrometer are those which are formed in a thin layer adjacent to the surface of the medium by the interaction of the energetic primary electrons with the atoms of the material. It appears from the observed constancy of the secondary electron yield per absorbed rad that the secondary electron yield is proportional to the energy deposited in the medium.

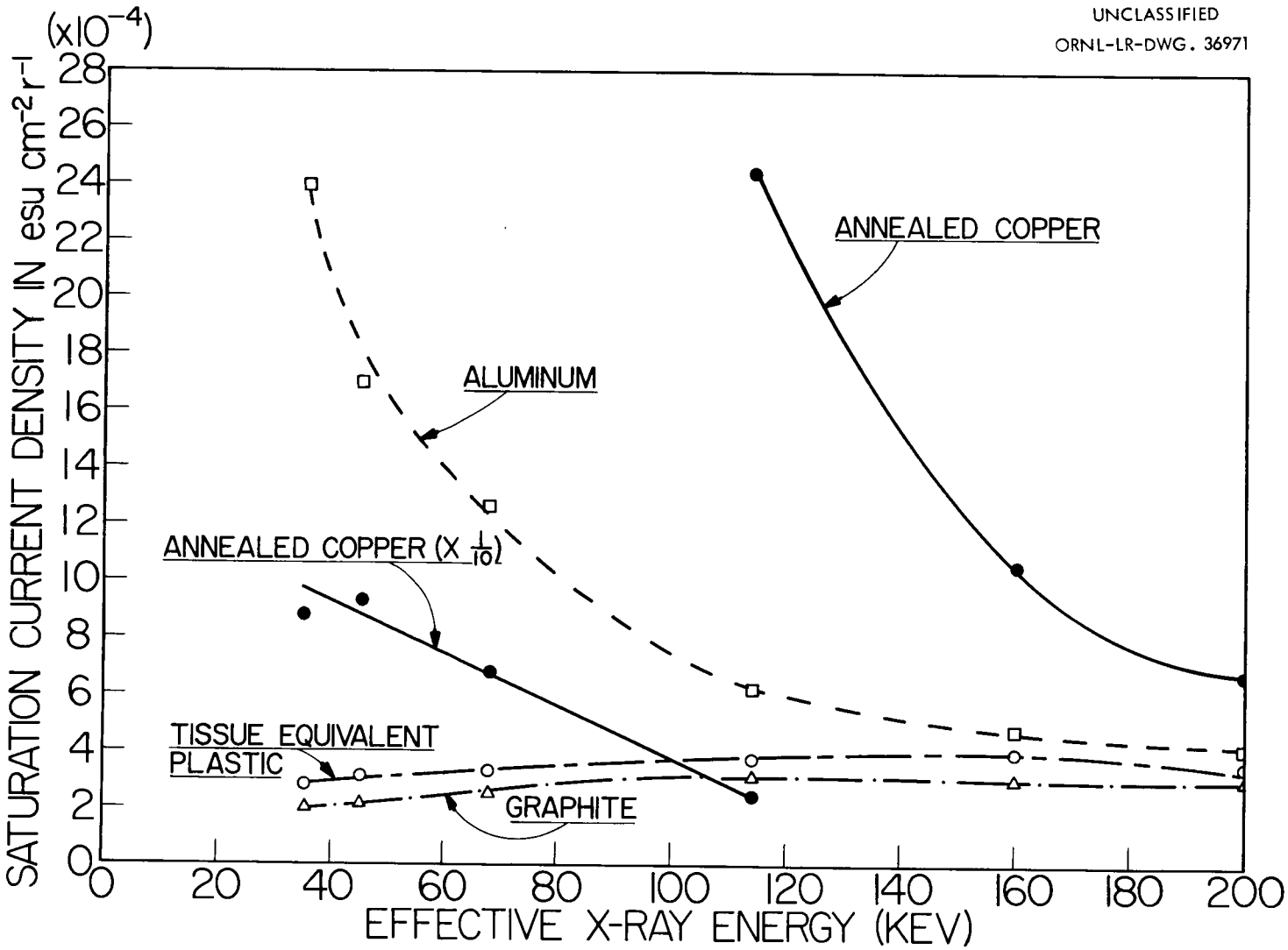

Fig. 23. Saturation Current Density per Roentgen for Heavily Filtered X-Rays.

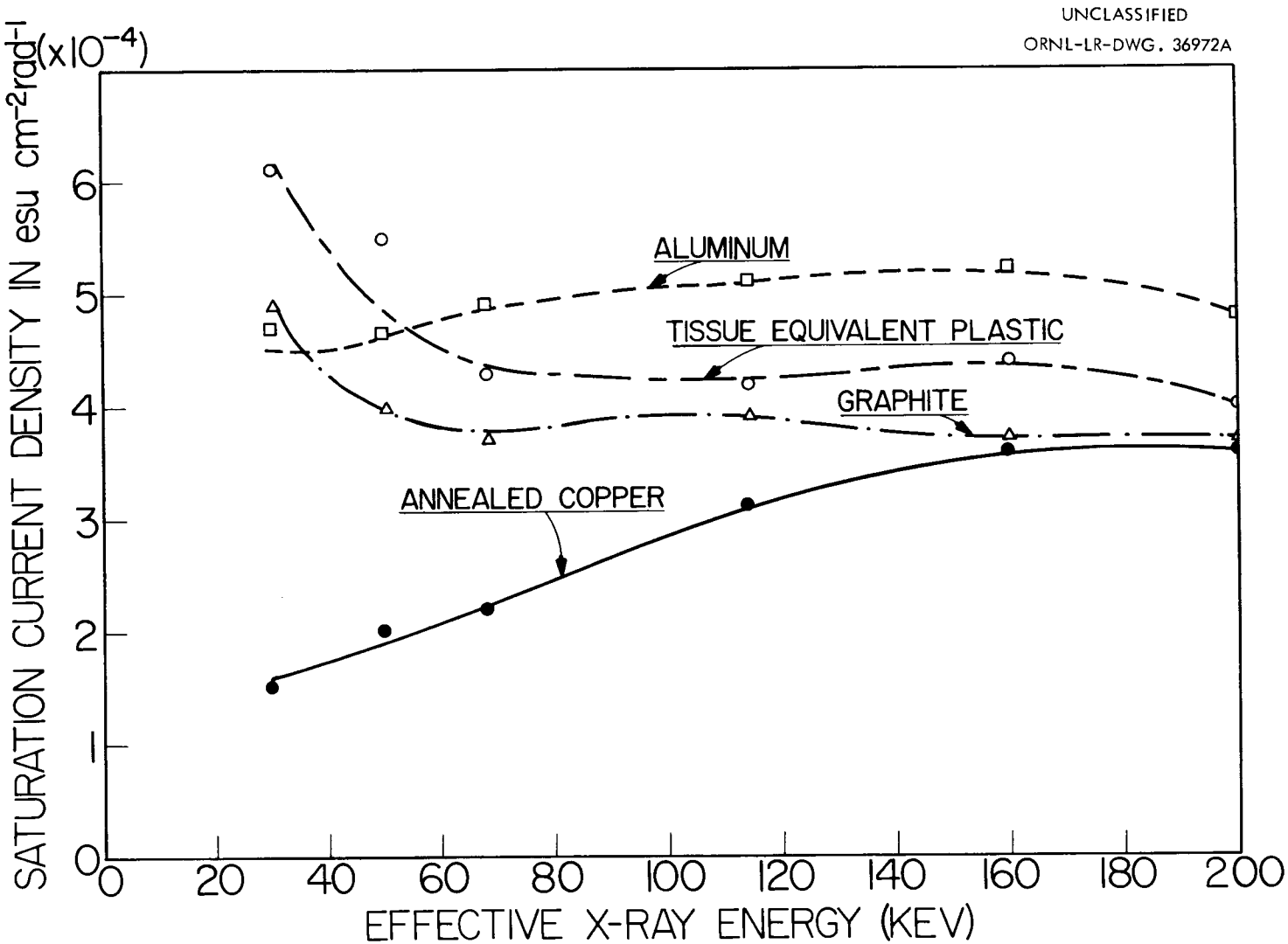

Fig. 24. Saturation Current Density per Absorbed Rad for Heavily Filtered X-Rays.

The dependence of secondary electron yield on energy deposition in the medium explains the phenomena previously noted for the flux spectra (section A). The difference in absolute magnitude of the electron spectra with different X-ray beams (250 and 180 KVCP), can be understood by considering the spectra as a function of absorbed dose (rad) rather than incident dose (roentgen).

VI. CONCLUSIONS

AC modulation of the bias was used to measure the second derivatives of the current-voltage curve of a parallel-plate spectrometer bombarded in vacuum by lightly filtered 250 and 180 KVCP X-rays. The secondary electron energy spectrum in theplate medium was shown to depend primarily on the second derivatives of the current-voltage curve. The spectra showed an increasing number of electrons at lower energies in the four plate materials measured: copper, aluminum, graphite, and tissue equivalent conducting plastic.

The energy distributions could not be fitted with a simple analytic function. Comparison with the function:

$$eN(E_w + V) = \frac{\alpha}{(\beta + E_w + V)^2} ,$$

found by Nelson showed good agreement for electrons with energies less than $(E_w + 6)$ electron volts, where E_w is the sum of the Fermi energy and the photoelectric work function. For higher electron energies, the distributions fall off more rapidly than the inverse square of the energy.

The total yield of low energy secondaries at saturation was found to be highly energy dependent, as a function of incident dose (r), for heavily filtered X-rays from 35 KeV to 200 KeV. However, the yield expressed as a function of absorbed dose (rad) was relatively constant for X-rays from 45 KeV to 200 KeV. Also, the yield (per rad) was of the same order of magnitude for the four materials and had a value of about $4.5 \times 10^{-4} \frac{\text{esu}}{\text{cm}^2 \text{ rad}}$.

APPENDIX I

Error Analysis

Random and systematic errors were considered separately in the experimental results. It was shown in Equation (75) that the absolute magnitude of the second derivative of the current-voltage curve was linearly related to the amplitudes of the AC input signals, the output beat-frequency signal, the gain of the pre-amplifier, the dose rate, the plate area irradiated, and the input impedance of the grid circuit. All but the latter two are subject to random error.

The random error in AC voltage measurements was assessed to be on the order of one per cent, the accuracy to which the scale of the wave analyzer could be read. Random error in the output beat frequency signal was calculated for each data point on the basis of the percentage of noise contained in the gross output. The percentage random error in the second derivative, d^2I/dV^2, at spectrometer bias voltage V, can be expressed as:

$$\left(\Delta_{d^2I/dV^2} \right)_V = \sqrt{(\Delta_g)^2 + (\Delta_A)^2 + (\Delta_B)^2 + (\Delta_r)^2 + (\text{noise/signal})_V^2} \qquad (81)$$

where Δ_g = error in determination of pre-amplifier gain = $\sqrt{(\Delta_{in})^2+(\Delta_{out})^2}$

$= \sqrt{(1\%)^2 + (1\%)^2} = \pm\ 1.4\ \%$.

Δ_A, Δ_B = error in input AC signal measurement = 1%.

Δ_r = error due to fluctuation of X-ray beam = 2%.

$\left(\frac{\text{noise}}{\text{signal}} \right)_V$ = percentage error in AC output measurement at bias V, due to noise signal.

The relationship between the energy distribution and the derivatives of the current-voltage curve was shown in Equation (12). It is evident that the first derivative enters into the energy distribution as an order of magnitude less than the second derivative. Thus, a maximum error of 10% in the calculated values of the first derivative would cause a 1% error in the energy distribution from this factor.

Systematic errors were estimates as:

Error in determining plate area irradiated	=	2%
Error in determining input impedance	=	3%
Error due to non-linearity between voltage scales of the wave analyzer	=	5%

The total systematic error can be expressed as:

$$\left(\Delta_{eN(E_w+V)} \right)_{sys.} = \sqrt{2^2 + 3^2 + 5^2} = \pm\ 6.15\% \qquad (82)$$

The systematic error was not included in the calculations or graphs of the energy distributions because it would not have altered the shape of the distributions. The random errors for each value V of bias are plotted on the energy distributions, as shown in Figures (16), (17), (18), and (19).

APPENDIX II

Table VII. Fermi Energy E_F and Photoelectric Work Function Φ for Cu, Al, Graphite, and Tissue Equivalent Conducting Plastic

	E_F(eV)	Φ(eV)	E_W(eV)
Copper[26]	7.00	4.45	11.45
Aluminum[26]	11.7	4.20	15.9
Graphite[27] and Tissue Equivalent Conducting Plastic*	~ 0	4.56	

* The values for the conducting plastic were assumed to be the same as for graphite since the plastic contained a large proportion of carbon (82% by weight).

[26] Dekker, A. J., SOLID STATE PHYSICS, (Prentice Hall, New York, 1957) p. 215.

[27] Taft, E., and Apker, L., Phys. Rev. 99, 1831 (1955).

Bibliography

Clemtentell, E., and Villi, C., "On the Imaginary Part of the Nucleon-Nucleus Potential", Nuovo Cimtimeto 2, 1, 176 (1955).

Dekker, A. J., SOLID STATE PHYSICS (Prentice Hall, New York, 1957).

Fairstein, E., "Grid Current in Electron Tubes", Rev. Sci. Inst. 29, No. 6, 524 (1958).

Fairstein, E., "Electrometers and Amplifiers", HANDBOOK OF INSTRUMENTS AND TECHNIQUES (To be published under sponsorship of the National Research Council Committee on Nuclear Science).

Fowler, H. A., Farnsworth, H. E., "Reflection of Very Slow Electrons", Phys. Rev. 111, No. 1, 103 (1958).

Gillespie, A. B., SIGNAL, NOISE AND RESOLUTION IN NUCLEAR COUNTER AMPLIFIERS, (McGraw-Hill Book Co., Inc., 1953) p. 22.

Goldberger, M. L., "The Interaction of High Energy Neutrons and Heavy Nuclei", Phys. Rev. 74, 10, 1269 (1948).

McGinnies, R. T., "Energy Spectrum Resulting from Electron Slowing Down", NBS 597, Superintendent of Documents, U. S. Government Printing Office, Washington, D. C. (1959).

Nelson, D. R., Birkhoff, R. D., Ritchie, R. H., and Hubbell, H. H. Jr., "Measurement of Electron Flux in Media Bombarded by X-rays", ORNL-2521, Oak Ridge National Laboratory, Oak Ridge, Tennessee (1958). Unpublished.

Platzman, R. L., "Subexcitation Electrons", Rad. Res. 2, 1 (1955).

Pol, Balth. van der, Weijers, Th. J., "Fine Structure of Triode Characteristics", Physica 1, 481 (1934).

Ritchie, R. H., Nelson, D. R., and Birkhoff, R. D., "Low Energy Collision with a Fermi-Dirac Gas", ORNL-2590, p. 110, Oak Ridge National Laboratory, Oak Ridge, Tennessee (1958). Unpublished.

Schottky, W., "Spontaneous Current Fluctuations in Various Conductors", Ann. Physik 57, 541 (1918).

Spencer, L. V., "Theory of Electron Penetration", Phys. Rev. 98, 1597 (1958).

Spencer, L. V., and Fano, U., "Energy Spectrum Resulting from Electron Slowing Down", Phys. Rev. 93, 1172 (1954).

Storm, E., Gilbert, E., and Israel, H., "Gamma-Ray Absorption Coefficients for Elements 1 through 100 Derived from the Theoretical Values of the National Bureau of Standards", LA-2237, Los Alamos Scientific Laboratory, Los Alamos, New Mexico (1958). Unpublished.

Taft, E., and Apker, L., "Photoelectric Emission from Polycrystalline Graphite", Phys. Rev. 99, 1831 (1955).

Taylor, L. S., "The Measurement of X- and Gamma Radiation over a Wide Energy Range", Brit. J. of Rad. 24, No. 278, 67 (1951).

Wolff, P. A., "Theory of Secondary Electron Cascade in Metals", Phys. Rev. 95, No. 1, 56 (1954).

ORNL-2732
Physics and Mathematics
TID-4500 (14th ed.)

INTERNAL DISTRIBUTION

1. C. E. Center
2. Biology Library
3. Health Physics Library
4-5. Central Research Library
6. Reactor Experimental Engineering Library
7-26. Laboratory Records Department
27. Laboratory Records, ORNL R.C.
28. L. B. Emlet (K-25)
29. J. P. Murray (Y-12)
30. A. M. Weinberg
31. J. A. Swartout
32. E. D. Shipley
33. M. L. Nelson
34. K. Z. Morgan
35. S. C. Lind
36. A. S. Householder
37. C. S. Harrill
38. C. E. Winters
39. A. H. Snell
40. E. H. Taylor
41. W. H. Jordan
42. T. A. Lincoln
43. A. Hollaender
44. F. L. Culler
45. H. E. Seagren
46. D. Phillips
47. M. T. Kelley
48. E. E. Anderson
49. R. S. Livingston
50. C. P. Keim
51. K. E. Cowser
52. C. D. Susano
53. L. B. Farabee
54. F. J. Davis
55. R. J. Morton
56. C. E. Haynes
57. E. G. Struxness
58. W. E. Cohn
59-109. H. H. Hubbell, Jr.
110. D. E. Arthur
111. J. Neufeld
112. M. J. Skinner
113. J. C. Hart
114. T. H. J. Burnett
115. W. J. Lacy
116. G. S. Hurst
117. T. E. Bortner
118. J. A. Lane
119. C. E. Clifford
120. J. L. Gabbard
121. R. A. Charpie
122. D. M. Davis
123. P. E. Brown
124. E. D. Gupton
125. J. C. Ledbetter
126. R. L. Clark
127. G. C. Cain
128. L. C. Johnson
129. W. W. Ogg
130. O. D. Teague
131. E. L. Sharp
132. E. J. Kuna
133. H. H. Abee
134. C. R. Guinn
135. A. D. Warden
136. C. C. Sartain
137. J. R. Muir
138. J. A. Auxier
139. M. F. Fair
140. S. I. Auerbach
141. G. W. Royster, Jr.
142. R. R. Dickison
143. F. W. Sanders
144. F. C. Maienschein
145. W. J. Boegly, Jr.
146. F. L. Parker
147. W. E. Lotz
148. B. Fish
149. M. B. Edwards
150. F. M. Empson
151. G. G. Robeck
152-201. R. D. Birkhoff
202. R. H. Ritchie
203. J. A. Harter
204. R. M. Johnson
205. W. G. Stone
206. J. S. Cheka
207. P. N. Hensley
208. R. W. Peelle

209. D. R. Nelson
210. E. B. Wagner
211. C. A. Preskitt
212. S. K. Allison (consultant)
213. W. H. Langham (consultant)
214. A. Wolman (consultant)
215. R. Zirkle (consultant)
216. L. S. Taylor (consultant)
217. ORNL - Y-12 Technical Library, Document Reference Section

EXTERNAL DISTRIBUTION

218-227. Mr. Roland A. Finston, 2949 Fitch Avenue, Chicago 45, Illinois
228. Knolls Atomic Power Laboratory, Schenectady (R. J. Feinberg, GE employee)
229. Industrial Reactor Laboratories, Inc., Plainsboro, N.J. (Andrew P. Hull)
230. Dr. Robert L. Platzman, Argonne National Laboratory, Lemont, Illinois
231. Division of Research and Development, AEC, ORO
232-771. Given distribution as shown in TID-4500 (14th ed.) under Physics and Mathematics category